ALMA MATER STUDIORUM ∼·∼ UNIVERSITÀ DI BOLOGNA

SCUOLA DI SCIENZE

DIPARTIMENTO DI FISICA E ASTRONOMIA

CORSO DI LAUREA IN ASTRONOMIA

Towards a Novel Concept of Imaging Spectrograph

TESI DI LAUREA

Presentata da:

Enrico BIANCALANI

Relatore:

Chiar.mo Prof. Daniele DALLACASA

SESSIONE II

ANNO ACCADEMICO 2016-2017

Contents

Bilingual Abstract

The objective of the present thesis is to introduce a novel concept of astrophysical light detector, which is capable of immediately analysing the spectral composition of two-dimensional images.

First of all, its breakthrough technology, which is based on the superconducting effect of kinetic inductance, is compared with the standard of semiconducting charged-coupled devices. They rely on the photoelectric effect and can only perceive the intensity of light over an exposure time by themselves, without dispersive elements or monochromatic filters in front of them.

In this context, I report on the result of my collaboration with the University of Oxford, where an integral-field spectrograph called KIDSpec is being developed, in the range that goes from ultraviolet to near infrared. It will be the first instrument of the sort built outside the USA. My task was to assemble an optical spectrometer tailored for a feasibility study of this apparatus. Then, the weaknesses of the optical system are briefly discussed, in view of its implementation.

What follows are the optical investigations whereby I inspected the performance of the spectrometer, with respect to its diffraction responses at various output angles and input wavelengths. In addition, an aetiology of the circle patterns caused by the employed optical fiber is provided.

Finally, a few possible astrophysical applications of the new kind of detector are reviewed: particular consideration is given to the emerging frontier of direct exoplanetary characterisation.

L'obiettivo della presente tesi è di introdurre una nuova concezione di fotorivelatore astrofisico, in grado di analizzare immediatamente la composizione spettrale di immagini bidimensionali.

Prima di tutto, la sua innovativa tecnologia, che si basa sull'effetto superconduttivo dell'induttanza cinetica, è confrontata con lo standard dei dispositivi semiconduttivi ad accoppiamento di carica. Essi contano sull'effetto fotoelettrico e possono solo percepire l'intensità della luce su un periodo d'esposizione, di per sé, senza elementi dispersivi o filtri monocromatici dinnanzi.

In questo contesto, riporto il risultato della mia collaborazione con l'Università di Oxford, dov'è in via di sviluppo uno spettrografo a campo integrale chiamato KIDSpec, operativo nella banda elettromagnetica che va dall'ultravioletto al vicino infrarosso. Sarà il primo strumento di tal sorta ad essere costruito al di fuori degli Stati Uniti d'America. Il mio compito consisteva nell'assemblare uno spettrometro ottico destinato ad uno studio di fattibilità di questo apparato. Quindi, le carenze del sistema ottico sono discusse in breve, in vista della sua implementazione.

A seguire, le indagini ottiche attraverso cui esaminai la prestazione dello spettrometro, quanto alle sue risposte in fatto di diffrazione, a varî angoli d'uscita e lunghezze d'onda in ingresso. In aggiunta, si fornisce un'eziologia dei motivi circolari causati dalla fibra ottica ivi impiegata.

Infine, sono esaminate alcune possibili applicazioni astrofisiche del nuovo tipo di rivelatore: particolare attenzione è data all'emergente frontiera della caratterizzazione esoplanetaria diretta.

Acronyms

ADC=Analog-to-Digital Converter

AO=Adaptive Optics

ArCONS=Array Camera for Optical-to-Near-infrared Spectrophotometry

CCD=Charge-Coupled Device

DarkNESS=Dark-speckle Near-infrared Energy-resolved Superconducting Spectrophotometer

DQE=Detective Quantum Efficiency

ELT=Extremely-Large Telescope

FDM=Frequency-Domain Multiplexing

FRD=Focal Ratio Degradation

FSR=Free Spectral Range

HST=Hubble Space Telescope

IFS=Integral-Field Spectrograph

IPRI=Integrated Pupil-Remapping Interferometer

KID=Kinetic-Inductance Detector

KIDSpec=KID Spectrograph

KRAKENS=Keck Radiometer Array using KID ENergy Sensors

MEC=MKID Exoplanet Camera

MOS=Metal-Oxide-Semiconductor

MUSIC=MUltiwavelength Submillimeter Inductance Camera

PICTURE C=Planetary Imaging Concept Testbed Using a Recoverable Experiment-Coronagraph

QE=Quantum Efficiency

SNR=Signal-to-Noise Ratio

WFPC=Wide Field and Planetary Camera

1 Prolegomenon

KIDSpec is a novel concept of spectrograph that has been designed to operate in the region of the electromagnetic spectrum ranging approximately from ultraviolet to near infrared. Its hallmark lies in the new superconducting technology of kinetic-inductance detectors (KIDs), which enables to measure the energy carried by single photons as well as each one's arrival time. As such, that instrument should be capable of directly revealing the spectral composition and the instantaneous intensity of incoming electromagnetic radiation, for two-dimensional images.

By contrast, the semiconducting charge-coupled device and its variations, representing the heart of many consumer and astronomical digital cameras, can only count the photons over an exposure time: in other words, the pixels of a CCD need some kind of dispersive element or monochromatic filter in front of them, to select a specific constituent of the polychromatic light. It's clear that skipping this intermediate step could reduce significantly the complexity and the weaknesses in the optical system of a telescope, leading to a revolution in the observational art.

The idea of microwave KIDs, called MKIDs, was conceived in 1999 at Caltech by Dr J. Zmuidzinas' team [36], which was focusing on X-ray astronomy. Then, one of Dr Zmuidzinas' coworkers, Dr B. A. Mazin, adapted the design to finally compete with CCDs in the optical [32]. Currently, optical arrays of KIDs with about 20 kpix are in their testing phase. Anyway, even a 2,024-pixel camera with a chromatic resolving power of about 10 gives evidence of the breakthrough, which can be appreciated in fig. 1. The major drawback is that KIDs work only if cooled around 100 mK, due to the superconductivity; a fact that makes them unwieldy for small spaces or spacecrafts, as well as for the commercialisation. But science is progressing quite fast.

2 CCDs versus MKID-arrays

As you can see, the image in the upper-left corner is far sharper than the other one: it was taken, in 2008, with the Wide Field and Planetary Camera 2, placed onto the Hubble Space Telescope. That camera contains four square CCDs with 640,000 pixels each, which operate simultaneously. Nevertheless, the two interacting ring galaxies of Arp 147[1] (440 Mly away from Earth) and their features, as well as the foreground star on the left (belonging to our Milky Way) can be still resolved with the 44×46-pixel camera ARCONS, which was installed in 2012 onto the 200-inch telescope of the Palomar Observatory. This is the first optical instrument based on MKIDs [18].

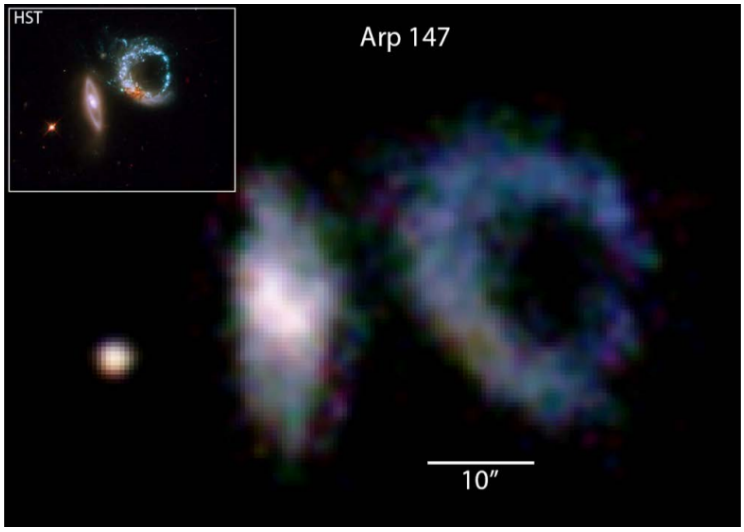

Figure 1 – Mosaic of Arp 147 taken with the ARCONS camera: KIDs are able to immediately capture the light spectrum. In the inset, a processed HST image for the same field of view: exposures with different filters are superposed [18].

[1] This is one of the 338 oddball galaxies compiled by Dr H. Arp in the Atlas of Peculiar Galaxies, in 1966 [1].

But, the key point here is that, in the former case, we are actually looking at a composite of monochromatic exposures made with infrared-, visible- and blue-light filters, each assigned with the appropriate RGB "false" colour [9]. Whereas, in the latter, the nature of each light beam is unaltered while it passes through the observing optics and gets focused onto the single MKIDs. 36 pointings of one minute each were performed and, only at a later time, each of them was calibrated and divided into three wavelength bands, to be assigned with the appropriate RGB values. Then the data were combined together and processed into the final image exhibited [18].

2.1 Electromagnetic Radiation

Before going into the details of the two technologies, let's have a briefing about the dual nature of electromagnetic radiation. Usually, it's regarded as a superposition of monochromatic and approximately plane waves that undergo phenomena such as interference and diffraction. This is a classical description and, for example, it will subtend the practical analysis given in section 3.

First of all, waves can be defined as perturbations applied to a certain function of space and time. They carry some energy, but no matter, while propagating through a medium—a Mexican wave of spectators, who stand up in successive groups and sit down without leaving their seats, exemplifies this concept. Each of them consists of an electric and a magnetic field that oscillate perpendicularly to each other, in a plane orthogonal to the direction of propagation: they are transverse waves as well. Therefore, the two fields behave like two harmonic oscillators, since they follow a sinusoidal law with the frequency ν characteristic of the electromagnetic radiation.

Our polychromatic radiation can be considered a system of these harmonic oscillators, which were found to be quantised by Dr Max Planck[2], in 1900. In addition, according to the theory of quantum mechanics, they are associated with a "gas" of massless bosonic particles called photons: these are nothing less than the energy packets, known as quanta, activated by the oscillators themselves. Every quantum of light transports a discrete amount of energy $h\nu$, where h is the Planck constant. The operating principles of both CCDs and MKIDs, i.e. the photoelectric and the kinetic inductance effect, are hinged upon this modern description of physical reality, which embraces light besides matter in a more penetrating way with respect to the classical one.

To quote from the speech held by Dr C. W. Oseen in 1929, on the occasion of the Nobel Prize Award Ceremony in honour of Dr Louis de Broglie, "for his discovery of the wave nature of electrons" [11]: "Hence there are not two worlds, one of light and waves, one of matter and corpuscles. There is only a single universe. Some of its properties can be accounted for by the wave theory, others by the corpuscular theory" [6]. To summarise, our oscillators and photons can be thought as two sides of a single coin: thus they express the wave-particle duality of light.

2.2 The Charge-Coupled Device

Dr W. S. Boyle and Dr G. E. Smith conceived the CCD in 1969 at Bell Laboratories, New Jersey, as an electronic memory. In 1976, it was first used as a light detector on the 61-inch telescope of the Lunar and Planetary Laboratory outside Tucson, Arizona, to take some images of Jupiter, Saturn and Uranus. Since then, the CCD has revolutionised the practice of optical observational astronomy [49]: by the end of the century, they were already able to measure objects a billion times fainter than the naked eye can see. In 2009, the two inventors shared half of the Nobel Prize in Physics, "for the invention of an imaging semiconductor circuit—the CCD sensor" [11].

[2]The Nobel Prize in Physics of 1918 was reserved until the following year and, then, awarded to Max Planck "in recognition of the services he rendered to the advancement of Physics by his discovery of energy quanta" [11].

Essentially, a CCD is a matrix of metal-oxide-semiconductor (MOS) capacitors. Each of these is a three-layer device consisting of a p-type semiconductor, an insulator and a thin metal coating. The semiconductor is usually doped *Si*, in which impurities have been added to make the (positive) electron holes the majority charge carriers: this is connected to the ground, on one side. The insulator is usually SiO_2 and forms the middle of the sandwich, in fig. 2. The metal on the other side is held at a positive voltage—a few volts, ordinarily. This positive voltage causes a depletion region devoid of electron holes to occur, in equilibrium, adjacent to the insulator. On the other hand, the minority charge carriers—i.e. the electrons—here are immobile, trapped in this potential well. During an exposure, when an incident photon above a certain cut-off frequency is absorbed in the depletion region, it generates an electron-hole pair, for the photoelectric effect[3]. The pair is swept apart before the two components recombine and the electron is stored in the potential well. The electron hole, in the meanwhile, leaves the material to ground. Eventually, if enough electrons accumulate in the depletion region, they neutralise the effect of the positive voltage and remove the potential well for newly generated electrons. It's the condition of saturation, whereupon electrons and holes start recombining [49].

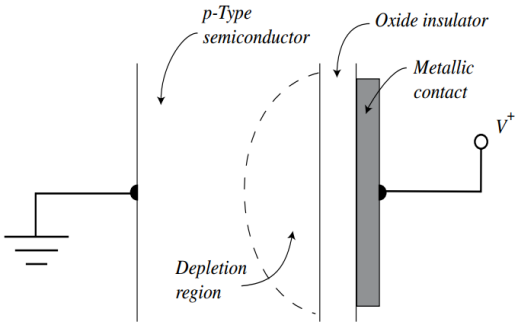

Figure 2 – Cross section of the physical structure in a MOS capacitor, the core of each CCD's pixel [49].

Over an exposure to light, the so-called photoelectrons are stored in the MOS capacitors, at the core of the picture elements (or pixels) of the CCD, at a rate proportional to the one of photon arrival (more or less). Then, a charge-coupling mechanism allows to shift the electrons to the neighbouring pixels, by sequentially manipulating depth and location of the potential wells. As you can see in fig. 3, the negative charges move only along the columns of the matrix, which form the parallel register, until they reach a transverse row (the serial register), shielded from light, from where they are read out. At this point, the electric charge is converted into a voltage, through a series of output amplifiers. The electric voltage is, in turn, converted into a binary number by the analog-to-digital converter (ADC) and, finally, saved in a computer memory [49].

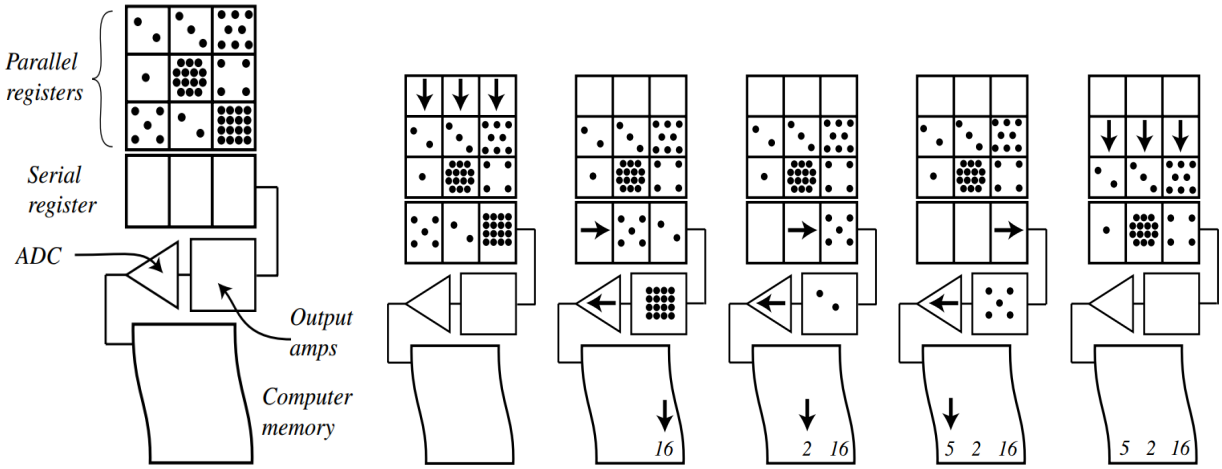

Figure 3 – The charge-coupled device at work. From left to right, the digital read-out of the photoelectrons [49].

[3]The Nobel Prize in Physics of 1921 was reserved until the following year and, then, awarded to Albert Einstein "for his services to Theoretical Physics, and especially for his discovery of the law of the photoelectric effect" [11].

Let's browse through the features for which optical astronomers long since settled on the CCD. HST is a billion-dollar telescope, so "it seems perverse if a detector does not use a large fraction of these expensive photons to construct its signal" [49]. The quantum efficiency has been defined as the fraction of photons that contribute to the signal, with respect to the incident ones. The camera that I've used in my optical investigations—Atik 460EX—contains a Sony ICX694 Exview sensor with a QE of 77% at 560 nm [13]. By contrast, the "specialized astronomical photographic emulsion Kodak IIIaJ achieved a QE of 3%, and the complex hypersensitizing process was used to boost the QE of emulsions up to 10%" [41].

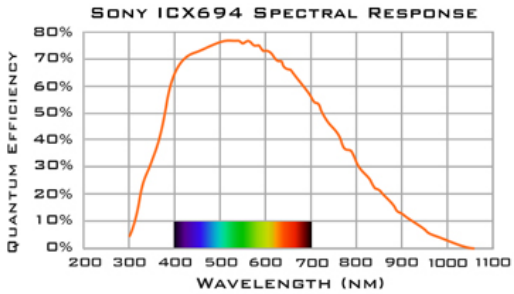

Figure 4 – QE of the CCD sensor in our Atik 460EX [13].

The uncertainty on the QE is determined by two causes: the imperfection of the detectors and an uncertainty intrinsic to the process of counting photons. If these are considered to arrive independently, but at a definite average rate, the latter can be modelled through the Poisson distribution: $\sigma = \sqrt{N}$, N being the number of counted photons. A quantity known as detective quantum efficiency takes into account the noise produced by the detector, besides this "Poisson noise", as well as the fact that not every absorbed photon get detected, according to the formula:

$$DQE = \frac{SNR_{out}^2}{SNR_{perfect}^2} = \frac{\left(N_{out}/\sigma_{out}\right)^2}{\left(N_{in}/\sigma_{in}\right)^2} = \frac{\left(\sqrt{N_{out}}\right)^2}{\left(\sqrt{N_{in}}\right)^2} = \frac{N_{out}}{N_{in}}, \tag{1}$$

where N_{out} is a fictitious number of photons: the number that a perfect detector would have to count to produce a signal-to-noise ratio equal to SNR_{out} [49]. For any detector, DQE $\leq$ QE ≤ 1. The DQE takes values of the same order of the QE, both for CCDs and photographic emulsions.

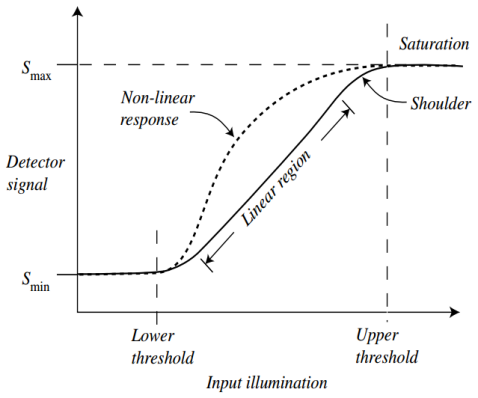

Figure 5 – Response curve of generic light detectors [49].

Fig. 5 illustrates the maximum range over which a detector gives an output in response to an input illumination. The human retina has a dynamic range of about 15,000 to 1: in fact, we can recognise objects both in the starlight and in bright sunlight. Anyway, its instantaneous one is quite limited, since the eyes take time for the adaptation to a different illumination environment. Photographic emulsions have a dynamic range of about 100 to 1; whereas, CCDs can go up to a ratio of 100,000 to 1, over a single observation [41]. Another crucial aspect of a detector is its capacity of giving an output signal directly proportional to the input illumination: the linearity. CCDs stay in the linear regime over a wide dynamic range. Problems are encountered towards the saturation—unless only a small region, surrounded by a low average light level, is overexposed—and nonlinear under extremely low intensity; but, this can be calibrated. By contrast, the photographic emulsion and the human eye give a logarithmic response, difficult to calibrate: the possibility to digitise the signal is another major advantage. One category where photographic plates could beat CCDs is the size; but, the latter can be arranged in a grid, as in the HST. Without considering their broader spectral response—much more than in our cones and rods—and their higher and tunable time resolution.

2.3 Microwave Kinetic Inductance Detectors

"MKIDs have been called the ideal detectors—like an X-ray microcalorimeter, they count single photons and measure their energy without read noise or dark current, and with nearly perfect cosmic-ray rejection" [29]. They are LC resonant micro-circuits composed of a superconducting inductive meander and an interdigitated capacitor in parallel with it. Some feedlines, capacitatively coupled to the inductors, slither across an MKID-array: their role is to input a probe signal at the frequency of microwaves. Square microlens are needed to focus light on the photo-sensitive inductors, due to the current QE. The working principle of these arrays implies a relatively simple design, if compared to the charge-coupling apparatus of CCDs: they offer zero read noise. Moreover, the low temperature of operation (read-out excluded) required by the superconductivity allows to minimise the noise coming from the "dark current", because thermal quasiparticles decrease exponentially with decreasing temperature. By contrast, CCDs can be cooled down to about 100 K. Also the detection itself is quantitatively and qualitatively different for the two detector types. Integrated circuits based on *Si* have an energy band gap of about 1.1 eV, which limits the quantum yield of a photon to an electron-hole pair, more or less, depending on its energy. On the other hand, superconductors have gap energies roughly 10,000 lower than semiconductors [10]. Many more electrons/holes are excited even by a weak photon, which eliminates the problem of false counts; it allows a harmless removal of cosmic rays as well. In addition, it opens up a wide simultaneous radiation window that ranges from about 0.1 µm in the UV to beyond the NIR from space, with a good QE—which decreases thorugh the infrared, as the absorbing metal films become more reflective [24]. This is the right spectral band to study exoplanets by direct imaging. By contrast, CCDs are limited to the range illustrated in fig. 4—the lower threshold for them is due to multiple electrons being promoted to the conduction band. Furthermore, the energy of the single photon can be determined by analysing the strength of its impact on the detector's complex surface impedance. And its arrival time too, with microsecond accuracy—MKIDS have no integration-time limit. As reported in the table below [29] the energy resolution (or chromatic resolving power) $R = \frac{\lambda}{\Delta\lambda}$ could be pushed up to a few tens with KRAKENS, the future evolution in the progeny of ARCONS. The raw yield of an MKID-array, as well as its dimension, are only a question of exploring the huge engineering phase space still uncharted. "The primary attraction of MKIDs is that, unlike many other low temperature detectors, they are easy to multiplex into large arrays" [25]. The elements of a resonator can fabricated with slightly different dimensions, so that they own a unique resonant frequency as well. A technique known as FDM, which allows to couple even a huge number of resonators to the same and only coaxial cable, to read them out simultaneously, thanks to the high quality factor of the resonator.

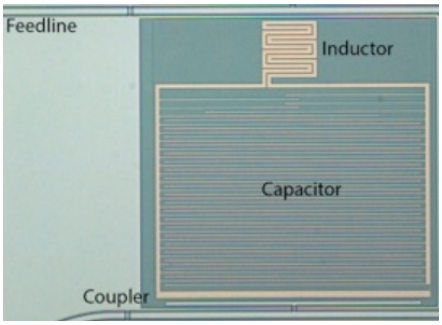

Figure 6 – A KID, made up of a 60 nm-thick *TiN* film, linked to a microwave feedline [10].

Name	ARCONS	KRAKENS Req.	KRAKENS Goal
Plate Scale	0.45 "/pixel	0.3 "/pixel	0.3 "/pixel
Pixel Count	2024	32400	32400
Fraction of Functional Pixels	70%	85%	95%
Field of View	20×20"	54×54"	54×54"
Maximum Count Rate	1000 cts/pixel/sec	1500 cts/pixel/sec	2500 cts/pixel/sec
Energy Resolution	R=10 at 0.4 μm	R=15 at 0.4 μm	R=25 at 0.4 μm
Cryostat Optics Throughput	<50%	65%	75%
Mean MKID Quantum Efficiency	30%	30%	80%
Wavelength Coverage	0.4–1.1 μm	0.37 – 1.1 μm	0.32 – 1.35 μm
Cryogenic Base Temperature Hold Time	12 hours	12 hours	16 hours

The Kinetic Inductance Effect

This superconducting phenomenon represents the real innovation of kinetic-inductance detectors, with the potential to subvert the status quo in the field of optical imaging (and) spectrography. Just like charge-coupled devices took the place of photographic plates, about 40 years ago. Below a critical temperature, the supercurrent in a superconductor is carried by electrons/holes coordinated in boson-like particles known as Cooper pairs[4]. This takes place via the mediation of nearby phonons, the quantised vibrational excitations of the surrounding ions. These "pairs" are said to condense into the fundamental quantum state, whereby they all have the same wave function: it results in a minimally-dissipative as well as ordered motion for direct supercurrents. What happens is that an electron passing through the ions of the atomic lattice leaves a wake of concentrated positive charge behind, because heavy ions move more slowly than electrons. This region attracts another electron, which comes to effectively form a sort of pair with the former. In turn, that will attract another electron through the same process, and so on. For this domino effect to occur, it's necessary that the electron-phonon coupling is stronger than the long-range Coulomb interaction between electrons. But, each of these electrons is effectively screened by a sort of electronic cloud, which embraces it, to shape a symbiotic entity known as quasiparticle [28].

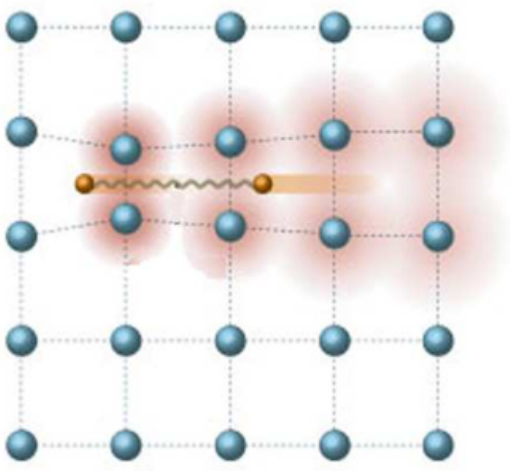

Figure 7 – Two electrons (orange) bound through the excitement of the atomic lattice they are immersed in [21].

Impedance generalises resistance for alternating currents: the surface impedance of the superconducting thin-film inductor, part of the resonator, is not null below the critical temperature. It's a linear combination of two terms: the surface resistance and the surface inductance component. The latter is named kinetic inductance because it arises from the inertia of the charge carriers opposing the varying electromagnetic field. In our case, the kinetic inductance has the leading role thanks to the so-called Bose-Einstein condensation which has just been introduced.

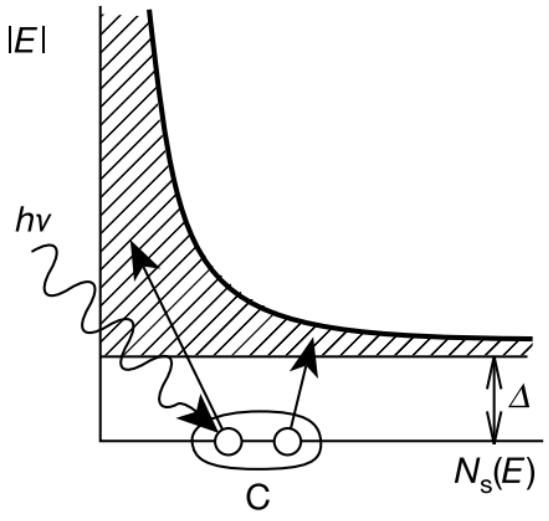

Figure 8 – The principle: breaking the Cooper pairs [24].

Semiconductors are characterised by excitation energies much higher than their superconductive ones: the 1.1 eV band gap for *Si* is outclassed by a factor of roughly 10,000 [10]. Therefore, an incident photon with an energy $h\nu \geq 2\Delta$, where Δ is the superconducting gap energy, break many Cooper pairs and generate a number of quasiparticles directly proportional to its frequency ν, except for a small portion of energy that ends up in phonons. A fact that affects both the surface kinetic inductance and resistance of the detector. Fig. 8 shows a Cooper pair (C) at the Fermi level; the shaded area is the density of states for quasiparticles ($N_s(E)$), as a function of their energy.

[4]The Nobel Prize in Physics of 1972 was awarded to the trio that cast John Bardeen, Leon N. Cooper as well as John R. Schrieffer "for their jointly developed theory of superconductivity, usually called the BCS-theory" [11].

Tangibly, the absorption of pair-breaking radiation induces a downward shift in the resonant frequency of the LC micro-circuit, as you can see in (a), below. On top of that, the increase in the density of quasiparticles leads to a larger dissipation, due to the interaction of these with the ions of the lattice. The surface resistance becomes relevant and undermines the on-resonance transmission dip, which results broader and shallower, as in (b): high transmission away from resonance emphasizes this aspect and makes the frequency-domain multiplexing profitable [24].

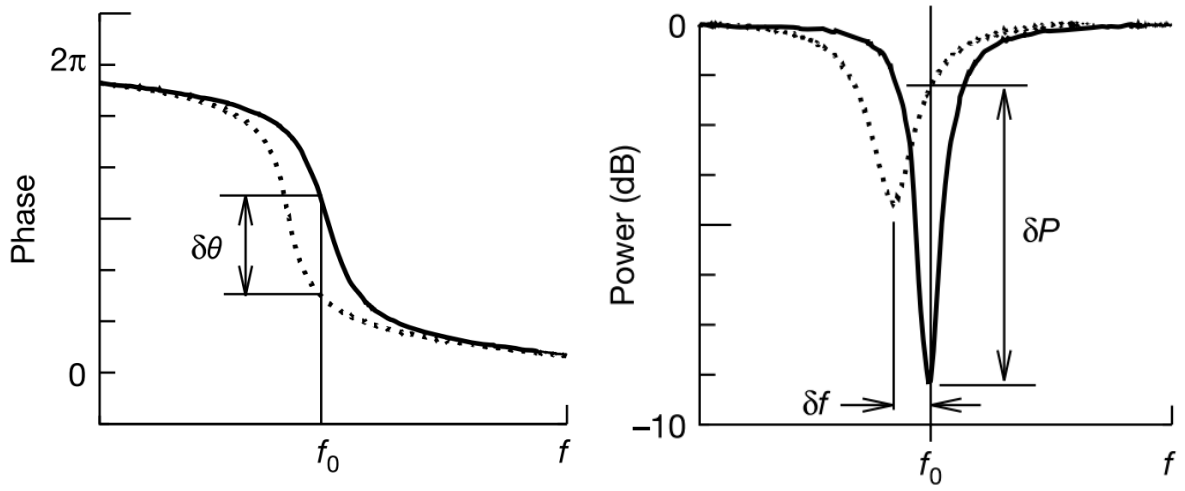

(a) Typical phase shift due to single-photon events [24]. (b) Typical amplitude shift, due to a single photon [24].

Figure 9 – A photon incident on an MKID affects the phase and the amplitude of the microwave probe signal [10].

In particular, every resonator imprints a record of its illumination on the sine wave that has a frequency corresponding to its resonant one. What constitutes the input signal is a comb of sine waves, each tuned to individual resonators, whose alteration is then digitised and analysed [25].

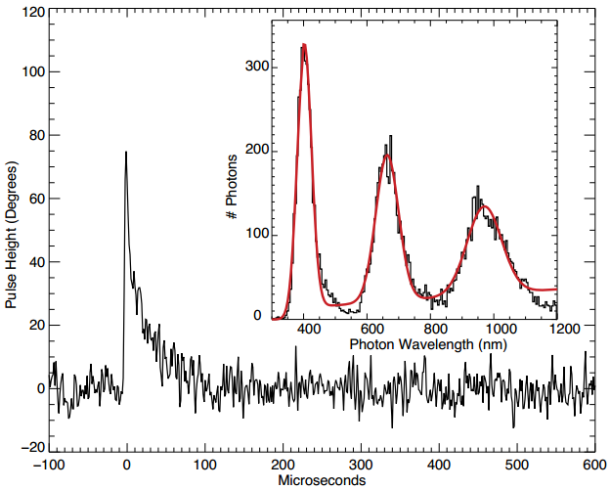

Figure 10 – A single 671.0 nm photon being absorbed by a *PtSi* MKID with $f_0 = 4.876$ GHz. The fitted quasiparticle recombination time is (36 ± 2) µs. The inset shows the spectrum of the same MKID that has been illuminated with lasers of 406.6, 671.0, and 982.1 nm. The data is transformed from phase height into wavelength, using these known laser wavelengths. The red line is a fit with three Gaussians and a linear background term, yielding a nearly uniform resolving power of 8 across the band [20].

Fig. 10 exhibits the phase shift of the probe signal caused by a photon with $\lambda = 671$ nm. The height of the pulse allows to measure the energy for the single quantum of light, to a few percent [23]. Quasiparticle excitations will persist until two of them meet and recombine into a Cooper pair, releasing a phonon, with a characteristic time-scale of few tens of microseconds: whereupon the fast-rise exponential-decay profile. The histogram in the inset reports the distribution of photons from three lasers of known wavelength, hitting the same MKID. The main noise source for KIDs is due to random fluctuations in the number of thermal quasiparticles. Unless the photon rate is too high and pulses get indistinguishable, the accuracy in determining their start time gives the accuracy of photons' arrival time. A feature that becomes essential in the observation of objects with a fast time variability: millisecond pulsars [24].

3 Towards a Feasibility Study of KIDSpec

The picture below encloses the product of my work. Once this optical system has been properly refined, it will serve as a monochromating tool in order to verify the feasibility of the imaging UV-to-NIR spectrograph named KIDSpec. In particular, the optical fiber end will be placed inside a cryostat, directly in front of one or more MKIDs, to provide the desired input illumination.

3.1 Setup of an Optical Spectrometer

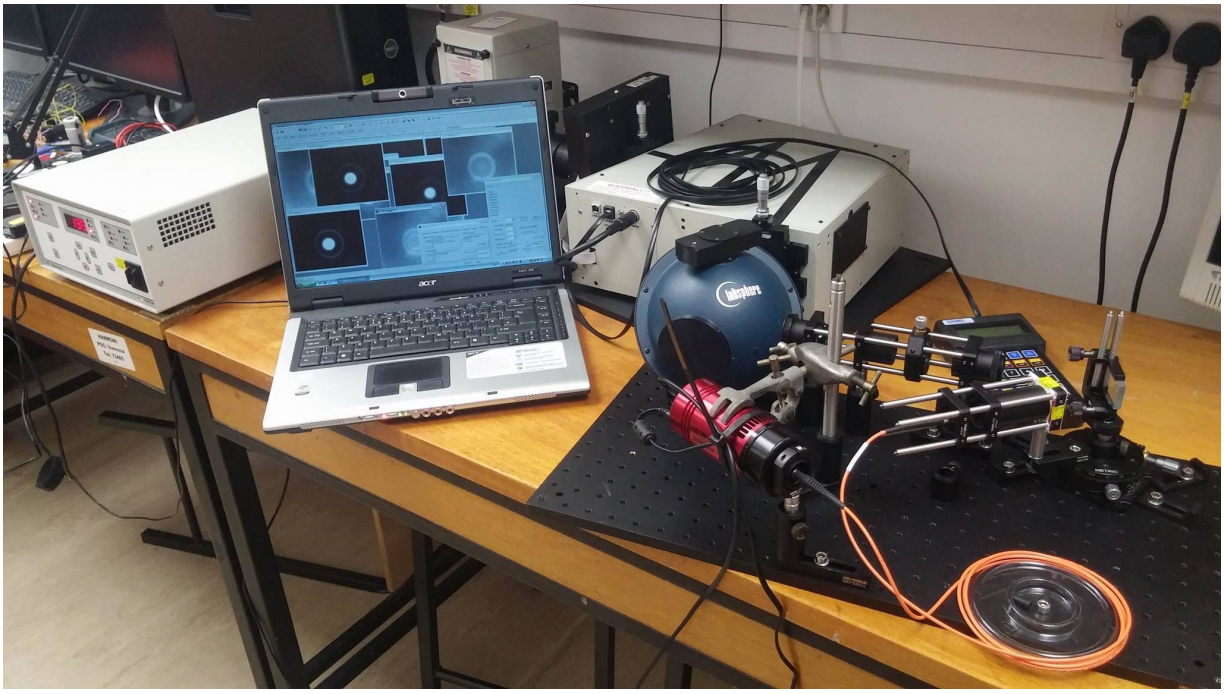

Figure 11 – My working table with the optical spectrometer linked both to a monochromator and to a CCD camera.

To the left of the PC, you can see the power supplier of a lamp located in the box behind the monitor. That feeds the monochromator linked to the system on the optical table. Its output is detected by a CCD camera and visualised on the same PC, through the programme *MaxIm DL*. What I built is an optical spectrometer, whose essential structure is illustrated by the next fig. 12. The desired electromagnetic radiation is directed by the monochromating tool into the assembled optics as an input image. Its component rays get collimated through the first arm, which leads to the blazed reflective grating. Instead of the initial slit, I introduced an iris diaphragm as an aperture stop, in front of the integrating sphere; then I added a glare stop, within the collimating system, in order to minimise the stray light. The second arm can move in front of the grating and intercept a minute range of wavelengths in its light, at a certain angle—hence, in a specific order—thus focusing those inside the core of the fiber.

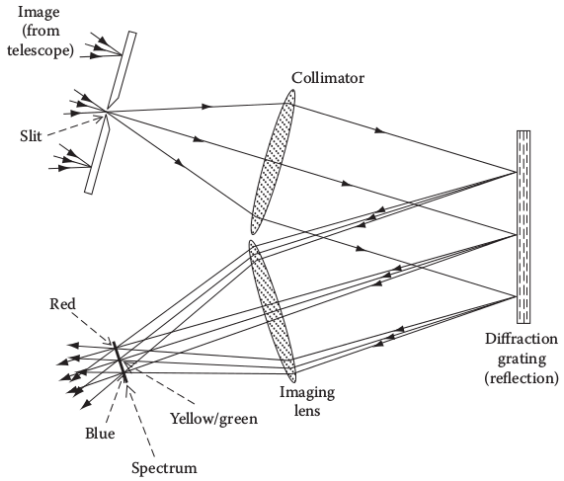

Figure 12 – Scheme of spectrometer similar to ours [38].

More in detail, the first element on the optical table is an integrating sphere by Labsphere. Its role is to scatter electromagnetic radiation in a diffuse fashion, known as Lambertian[5], and inject it into the spectrometer, so that the input intensity is independent of the observer's angle of view.

The principal arm comes next and points at the diffraction grating—which has been manually placed at the exit pupil—when viewed from above the integrating sphere, as in fig. 13. As mentioned above, it starts with a diaphragm, to adjust the amount of light leaving the sphere. Then, the collimator consists of a focusing lens followed by the collimating lens, with focal lengths of about 25.4 mm and 50.0 mm, respectively. It has a glare (known also as Lyot) stop in between, with an handmade aperture of the order of one millimeter. This should clean the focus of the former lens and define a sort of point source for the latter: to serve light as much collimated as possible to the grating and obtain a predictable output. I'll defer to the appendix B for the dimensional relations between the elements as well as an overall picture of the arrangement. As for the grating, Dr Mahashabde and I have created a structure ad hoc, in order to make its diffracting surface roughly pivot on the rotation axis of its rotating stage, which is the support of the second arm. In fact, it's necessary that this points at the same centre of rotation. The positioning accuracy of the grating can be enhanced with a standard optic mount.

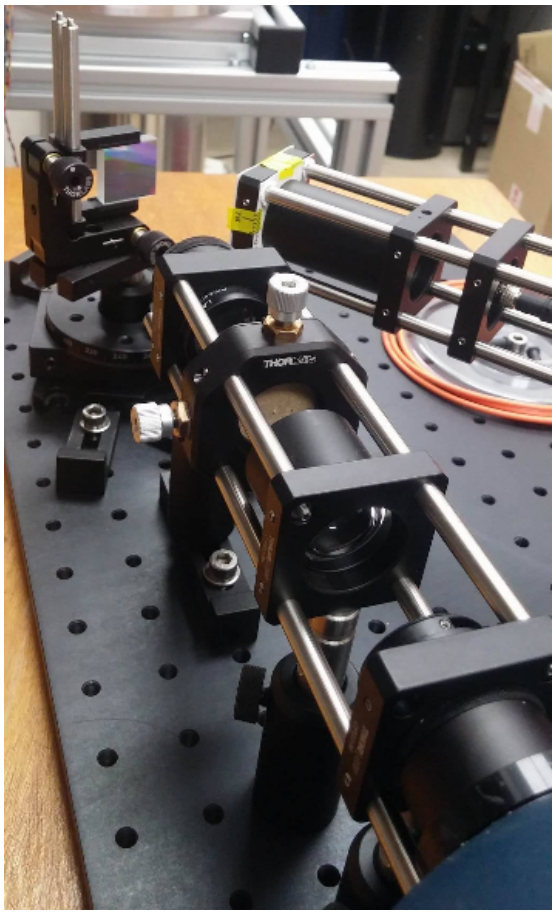

Figure 13 – In the foreground, the cage system that forms the main arm of the spectrometer, which is connected to the integrating sphere and is directed towards the grating.

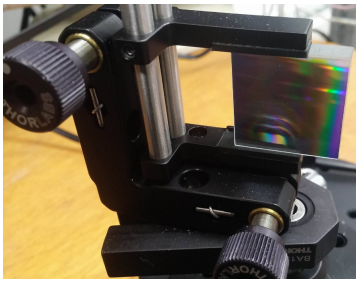

(a) The GR25-0310 grating.

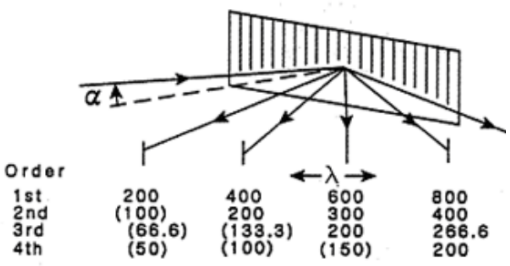

(b) $\lambda < 190$ nm is absorbed by air [8].

Figure 14 – In (a), the fluorescent tubes in the laboratory illuminate the grating. In (b), a generic diffraction chart.

[5]Dr Johann Heinrich Lambert (1728–1777) was a Swiss polymath. "He was the son of a small tailor, and had to rely on his own efforts for his education; from a clerk in some ironworks he got a place in a newspaper office, and subsequently, on the recommendation of the editor, he was appointed tutor in a private family, which secured him the use of a good library and sufficient leisure to use it", in the words of Dr W. W. Rouse Ball [37]. This was a British mathematician, lawyer as well as amateur magician: he was the main founder of the Cambridge Pentacle Club in 1919, one of the world's oldest magic societies, and continued as its (first) president until his death in 1925.

The secondary arm is designed to move around the grating, grabbing diffracted radiation of a minute range of wavelengths that goes in a certain order, at a certain angle. This occurs thanks to a camera lens focusing it into an optical fiber, which eventually illuminates the CCD camera.

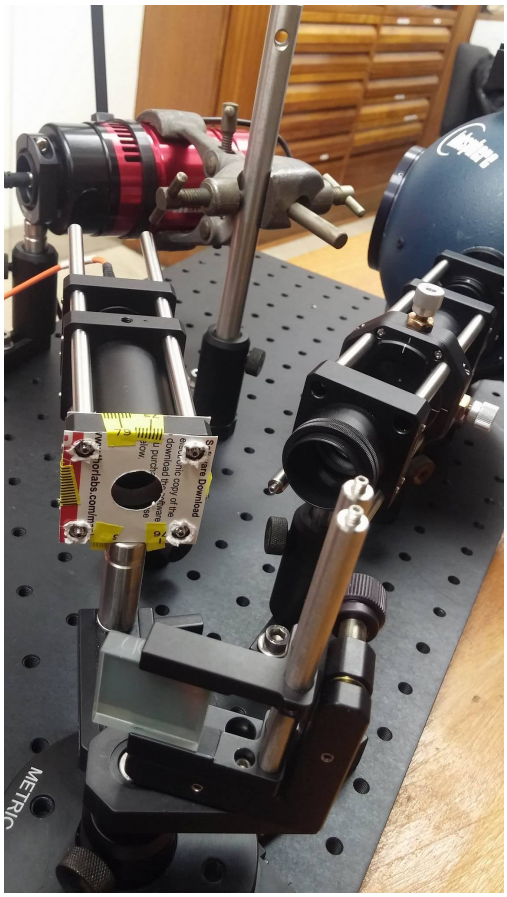

Figure 15 – The two arms converging on the grating.

It starts with two glare stops that are attached to the sides of a cage plate holding the relative arm, as you can see on the left of fig. 15. They limit electromagnetic radiation coming from undesired orders, as well as stray light from unintended reflections. After these, the camera lens is collocated at the end of a long tube: the fiber has been manually positioned at its focus. In fact, its input is secured to a cage plate that can move back and forth within a sort of four-stick rail. This feature is exploited for a tolerance study of the situation, reported in the appendix C. The output of the fiber and the aperture of the CCD camera are joint together, as in the background of fig. 15. From another perspective, in fig. 16, the disposition is clearer and the whole fiber cable is visible, coiled in the foreground. The rotating stage at the base of the grating, supporting the secondary arm, is visible as well: you could also notice that the diffracting surface is approximately centered on its axis of symmetry. Next up, let's point out the weaknesses of the optical spectrometer, in this final arrangement, in view of its subsequent improvement.

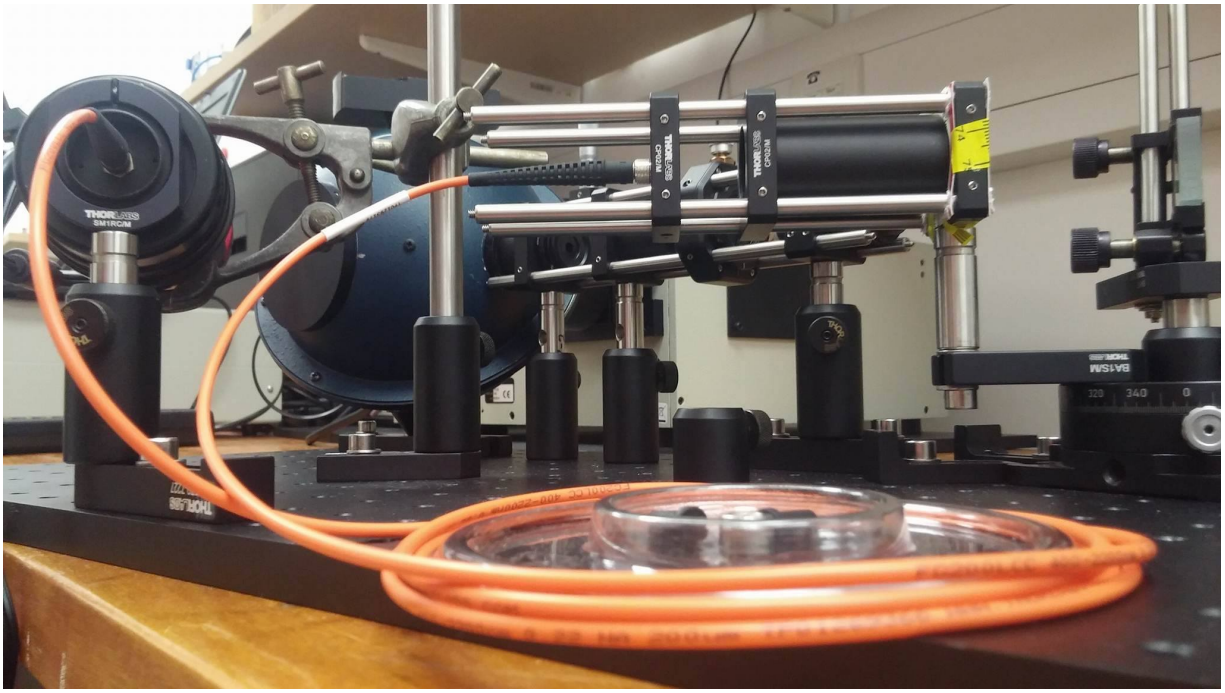

Figure 16 – The optical fiber links the secondary arm that is looking at the grating to the back of the CCD camera.

Weak Points of the Apparatus

As I will prove soon, the spectrometer previously described is ready to give some evidence of KIDSpec's feasibility, but it should be optimised in a few points, for a proper assessment of that.

First of all, there are some structural aspects of the assembled system that can be improved. For example, the reflective grating surface doesn't pivot precisely on the rotation axis of its optical post, which means less control on the diffraction pattern: a standard optic mount, instead of our ad-hoc solution, would be ideal. The position of the grating surface with respect to the previous optics has been qualitatively determined, in order to intercept the exit pupil coming from there: it should be established with more accuracy, after the other corrections. Then, the three field stops are hand-made and the location of the principal one, within the collimating system, has been qualitatively determined, again. Another point is that, by mistake, I chose the second of the mentioned lenses with a longer focal length than the other one, which translates into a larger beam out of the collimator, compared to the entrance one: so, the level of collimation is worse. Optical simulations in OpticStudio would be useful here, but probably superfluous for our objective: a practical testing of the instrument, with the suitable filters, should be enough for the next structural upgrade. Eventually, to be precise, the orientation of the first two lenses should be inverted: in fact, "when collimating a point source, generally the first air-to-glass interface should have the greater radius of curvature. Conversely, when focusing a collimated beam, the air-to-glass interface with the shorter radius of curvature should face the incoming beam" [15].

Secondly, a manufacturing defect of the deployed optics has been encountered during the following optical investigations. The building blocks of the system—especially tubes and sticks—reflect light more than they should: therefore, some annoying ghost images appear at the fiber input, resulting in spurious photons that disturb the desired diffraction pattern. A solution could be found in the "Blackout Materials", such as the masking tape—sold by Thorlabs, for example.

3.2 Diffraction and Gratings

Our plane of observation is far enough from the grating to allow for the Fraunhofer point of view, when analysing the diffraction effects of this, rather than the more general Fresnel theory. Let's consider a small aperture on an opaque screen Σ, illuminated by plane waves, from a distant point source. Fig. 17 shows what happens when moving a (parallel) plane of observation σ away from it. Close to the aperture, the projection of this onto that plane "is clearly recognizable despite some slight fringing around its periphery" [42]. These fringes, which come from the Fresnel or near-field diffraction, become more and more prominent with the distance, even in the center. "At a very great distance from Σ the projected pattern will have spread out considerably, bearing little or no resemblance to the actual aperture. Thereafter moving σ essentially changes only the size of the pattern and not its shape" [42]. As a rule-of-thumb, Fraunhofer diffraction occurs at an aperture of greatest width a, under the condition $R > a^2/\lambda$ [42]. Here, λ is the wavelength of the incident electromagnetic radiation. If reduced enough, this is sufficient to recall the Fresnel approximation, maintaining a fixed. R refers to the smaller between two distances: from the aperture to the point of observation and from it to an approximately point source—of the order of one millimeter, in my definitive setup.

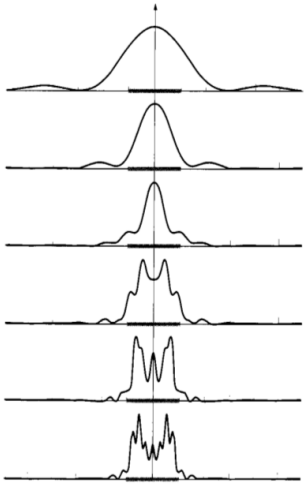

Figure 17 – From Fresnel to Fraunhofer, going from the bottom up [42].

"No single tool has contributed more to the progress of modern physics than the diffraction grating, especially in its reflecting form".

— Dr George Russell Harrison[6][34]

The employed diffraction grating is a repetitive array of grooves which gives shape to as many parallel bumps, having a saw-tooth profile. The aluminium coating on top of this structure reflects radiation falling on it and determines predictable periodic alterations in the phase (and not in amplitude, here) of the electric field, due to the spatial modulation of the refracting index. More precisely, it's an "echelette" ("small ladder" in French) grating, as named by Dr R. W. Wood (cf. footnote [12]) at the beginning of 1900 [33], to distinguish it from the echelon that Dr A. A. Michelson[7] used for his spectroscope, in 1898 [46]. The former has relatively low blaze angle and high groove density: therefore, it's capable of concentrating the radiation energy in the lower diffraction orders and providing a better spectral resolution, at the cost of the wavelength coverage. The "echelle" grating, first described by Dr G. R. Harrison, is a middle way between the two.

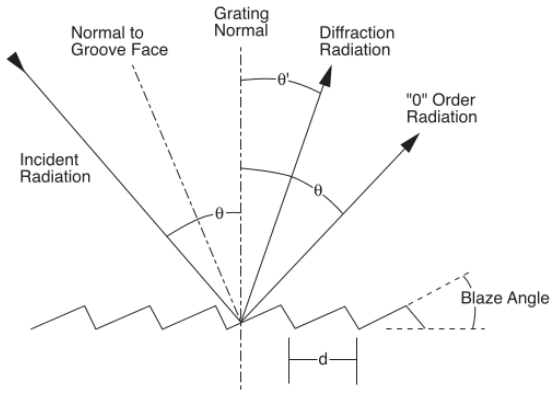

Figure 18 – Section of a ruled reflective grating. By convention, angles regarding light start from its normal [12].

By considering a monochromatic wave, there exists a unique set of discrete angles along which constructive interference occurs, once the groove spacing d is given. In these cases, the diffracted radiation from each tooth facet is in phase with the radiation diffracted from any other facet [39]. Blazing refers to the fact that diffracted radiation of a specific spectral region and order concentrates into an angular region that follows the law of reflection, when applied to the grating facets. If the angle of diffraction is equal in value and opposite in sign with respect to the incident one, the grating acts as a mirror and; in which case, polychromatic waves are not separated: the associated diffraction order is zero. Thanks to the saw-tooth profile, this contribution gets negligible. When the two angles in question are the same, the Littrow configuration applies, such as in the simulations reported in the appendix A: incident radiation is diffracted back from where it came.

Let's present the two important equations behind our next investigations on the spectrometer. The former is derived from first principles in [26], according to the scalar theory of diffraction, and governs the distribution of the diffracted light intensity with respect to the diffraction angle.

$$I = sinc^2\left\{\frac{m\pi\ cos\alpha}{cos(\alpha-\phi)}\left[cos\phi - sin\phi\ cot\left(\frac{\alpha+\beta}{2}\right)\right]\right\}, \tag{2}$$

where ϕ sets the blaze angle of the grating, α and β stand for the incident and diffraction angles, respectively—calculated from the grating normal, in our convention; and m refers to the diffraction order, for the principal light maxima. The radiation wavelength and β are interdependent. In fact, eq. (2) is implicitly related to λ, through the following equation, as illustrated in fig. 19.

[6]Leading figure of experimental physics at MIT from 1930 to 1979, he invented the echelle spectrograph in 1949 and "was the first to devise a practical ruling engine [...] which he used to produce diffraction gratings of unprecedented optical quality and size" (information taken from the History section in the website of the MIT Spectroscopy Laboratory, the first center of the sort, founded by Dr G. R. Harrison himself with Dr K. T. Compton).

[7]The Nobel Prize in Physics, in 1907, was awarded to Albert Abraham Michelson "for his optical precision instruments and the spectroscopic and metrological investigations [e.g. light speed] carried out with their aid" [11].

A geometrical derivation of it, which is known as the grating equation, can be found inside [39].

$$\lambda(\beta) = \frac{d\ (sin\alpha + sin\beta)}{m}, \tag{3}$$

where the parameter d is the distance between each pair of grating grooves, as illustrated in [12]. By simulating our grating with the software Grating Solver (GSolver), a realistic implementation of eq. (2) can be obtained—here, as a function of wavelength. The peaks of radiation intensity for the various orders follow the same trend—with a dip in the middle and slope towards lower wavelengths—of an aluminium coating, whereby our grating is covered. Note that, by plotting the SumR column—the sum over all the efficiency contributions in reflection (R), from different orders and for every wavelength—in the Results section of GSolver, it's possible to directly obtain an envelope similar to the reference curve (b). The regular reflectance refers to the ratio of specularly reflected radiant power—without diffusion—to incident radiant power. For this and the other simulations in the appendix A, the general Table refraction model has been employed.

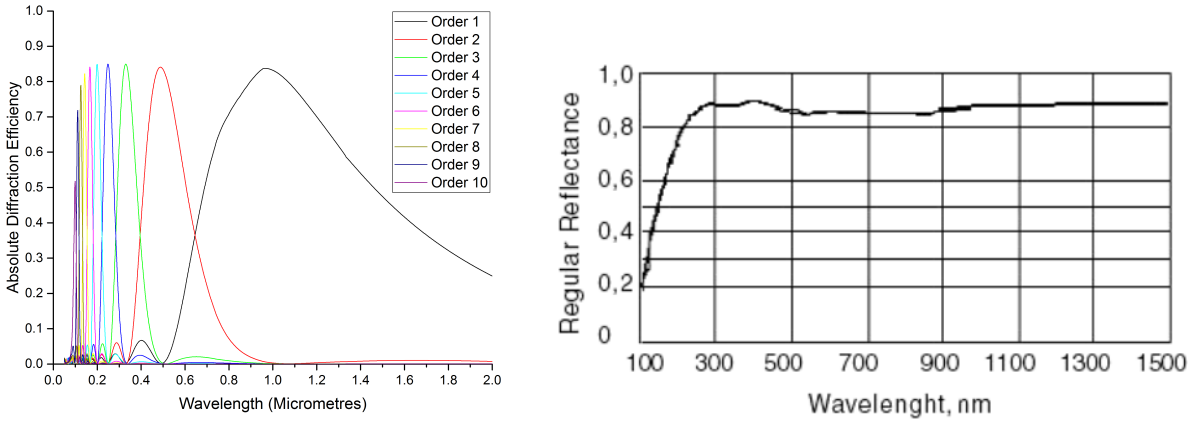

Figure 19 – In (a), the GSolver simulation of our grating's absolute efficiency, considering parallel polarisation and Littrow constraint, as well as a uniform input illumination. In (b), the spectrum of the reflectance—without diffusion—for an aluminium coating, such as the one that covers the top part of the deployed reflective grating [4].

"No one has ever been able to define the difference between interference and diffraction[8] satisfactorily. It is just a question of usage, and there is no specific, important physical difference between them" [47]. Under the premise, a representation of a bichromatic pattern resulting from several apertures is exhibited: diffraction gratings would give a similar response. Secondary maxima are neglected, here, to simplify the scene and display the order-dependence in the chromatic resolving power of the grating. Light distributes with a multi-slit interference pattern that's modulated by a single-slit diffraction envelope.

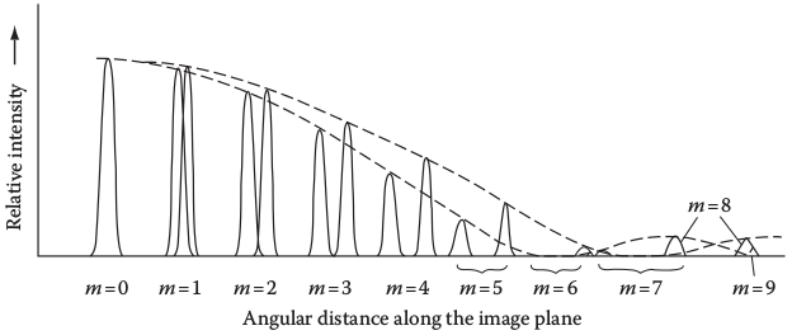

Figure 20 – Schematic angular distribution of the efficiency, for a single bichromatic point source viewed through small apertures, in front of it [38].

[8] As a curiosity, "to interfere" comes from the Latin *inter*, «between», and *ferir*, «to strike», through the Middle French. And it's properly used for horses that strike one leg against another. The English polymath Dr Thomas Young (1773–1829), "the last man who knew everything" [48], gave the term a physical sense. The word diffraction was coined by Dr Francesco Maria Grimaldi (1618–1663), a Jesuit priest and (astro)physicist from Bologna, in [45].

Other two crucial aspects resulting from certain manipulations of eq. (3), described in [39], are sketched out below. For higher orders and away from the grating normal, the angular dispersion of diffracted light, expressing the spectral range per unit angle, increases. In a sense, the opposite behaviour is kept by the free spectral range (FSR). This is the maximum spectral bandwidth that can be achieved, in a determined diffraction order, with no overlap from the adjacent orders: the superposition from the neighboring orders gets more and more significant as soon as the higher ones come into play.

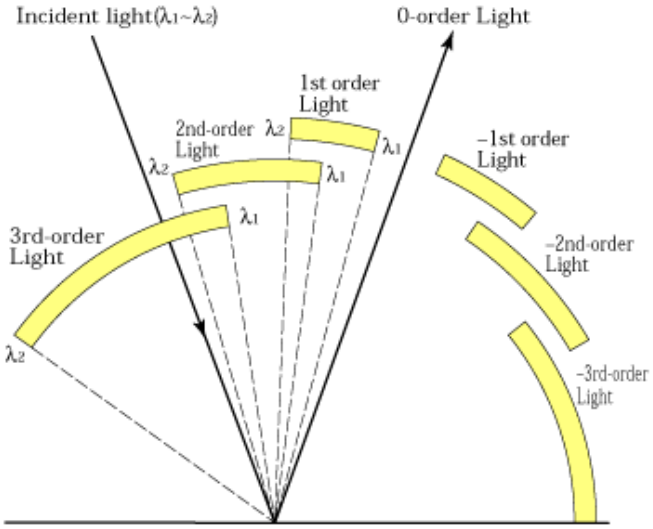

Figure 21 – The spectral behaviour of a reflective grating [14].

Optical Investigations

Beforehand, during the setup phase, I used a commercial laser pointer—Inateck WP1003—emitting light at about 650 nm. It was a guide to tip and tilt the reflective grating into the desired configuration. I also managed to correct a few hidden optics misalignments, in the primary arm. The 0^{th} order of the output radiation, intercepted by the card as the central dot in fig. 22, has been fixed at an angle of 15.48° from the grating normal. Since this corresponds to the condition of specular reflection, the angle between the normal and the incident radiation is as much. Moreover, the centers of the diffracted beams have been set to lie within the same plane, parallel to the optical table. Every red dot, representing the projection of a certain order for the mentioned wavelength, is horizontally aligned with the others. Note that the two dots visible on the white screen framed by the four-stick cage are closer together: they are focused by the imaging lens in front of them, at the beginning of the cage. In the final configuration, the secondary arm has been modified and moved on the other side of the main one. The grating and its arrow have been inverted to face the right-hand side—when looking at the grating from the integrating sphere—implying no change in the adopted sign convention.

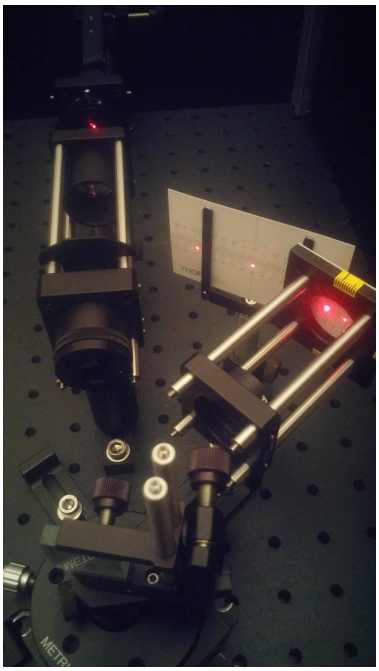

Figure 22 – Preliminary alignment.

Qualitative measurements were performed to test the agreement between the response of the optical spectrometer and the grating equation 3, which is represented by fig. 23. For example, the angles at which the previous red dots were found returned the correct wavelength, through eq. (3), with an accuracy of about half a degree. Precise measurements are obtained thanks to the vernier scale engraved on the rotating stage perimeter, having 5′-markings. In view of the following analysis, note that the given angles must be converted from the ones read on the rotating stage: exempli gratia, 39.5° corresponds to about 41.2°; 32.5° translates to about 48.2°.

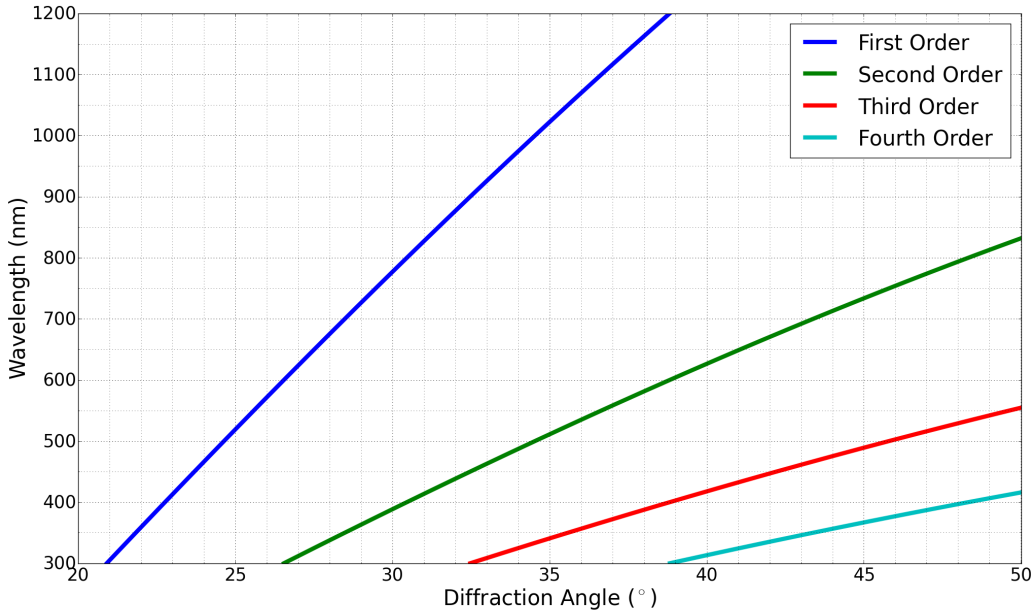

Figure 23 – Analytical graph of the grating equation 3, applied to our situation. Angles refer to the grating normal.

Here is one of the final images taken with our CCD camera, the Atik 460EX, through the programme MaxIm DL. The bar gives some reference electronic counts associated with the grey-scale intensities. The bar and the $\log_{10}$-scale are produced with the application SAOImage DS9.

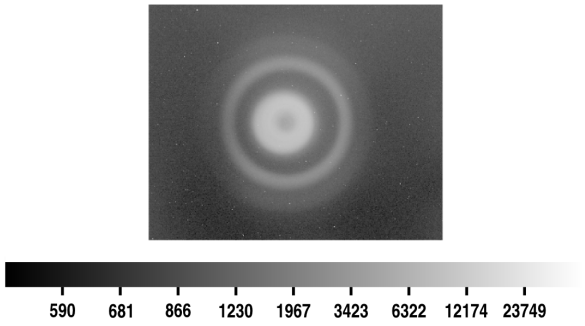

Figure 24 – A 50 s exposure to 544 nm light, at about 25.5° from the grating normal: i.e. the 1st diffraction order.

The secondary circle pattern is due to the so-called focal ratio degradation (FRD). Practically, this is the gradual increase of beam aperture along the optical fibre and makes the shape of the output beam fuzzy. It basically depends upon "the manufacture quality and the physical conditions at which the fibre is submitted" [2]. In other words, it deals with micro-bends and deformations at the interface between the core and the cladding, generated during the production process or later.

In fig. 25, a light beam with focal ratio $\frac{F}{D}$ =10 is launched into the fiber. The fiber output is distributed in cones with apertures $F/2.3$, $F/6$ and $F/10$: in this example, 40% of light is lost by FRD towards larger cones. Theoretically, all the electromagnetic flux should be within the numerical aperture (NA) of the fiber, inversely proportional to two times the focal ratio; but reality is different [2].

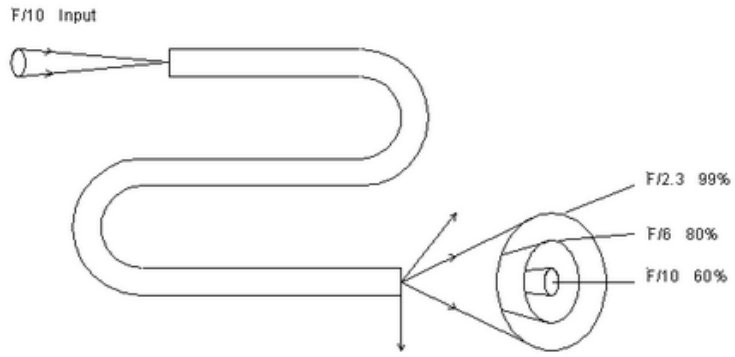

Figure 25 – Aetiology of the secondary circle pattern: the FRD of an input radiation, within a fiber duct, results in a beam spreading out at the end [2].

The main ring is produced by all those rays that go into the fibre not within one of the meridian planes intersecting its optical axis; and with an incidence direction not perpendicular to the entrance surface. As such, they are forced to spiral through the optical fiber and project a circle onto the flat detector intercepting them, at the exit. According to [2], most of the rays that enter a fiber are skew. In light of these features, let's have a look at a sample of images.

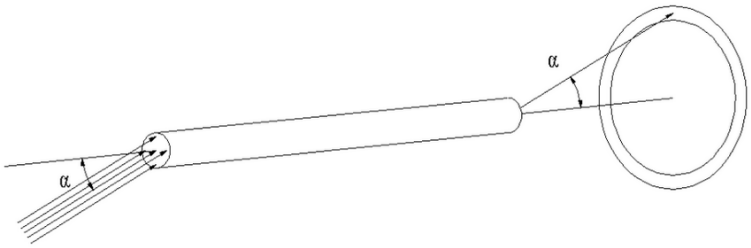

Figure 26 – Aetiology of the main ring of light: skew rays enter the fiber with an angle α and produce a ring having a radius set by α, at the end [2].

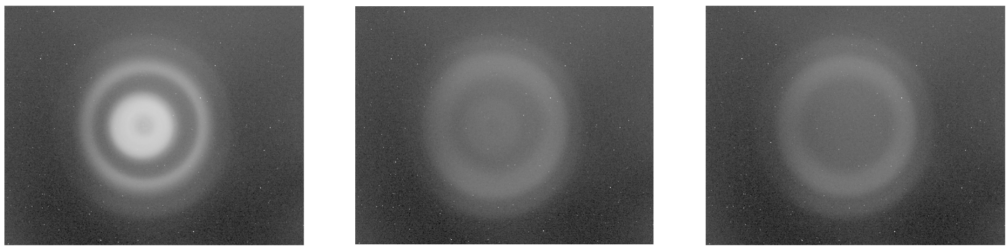

(a) 615 nm, in the 2nd order. (b) 410 nm, in the 3rd order. (c) 307 nm, in the 4th order.

Figure 27 – 50 s exposures to three wavelengths. The angle between the arm and the grating normal is about 39.5°.

It turns out that images (a) and (b) of fig. 27 are in agreement with the expectation. On the other hand, image (c) is missing the central structure, which should be at least as bright as the one in (b), according to fig. 28. It could be a problem of the analytical simulation, not being realistic enough; or a misalignment of the secondary arm, not looking accurately enough in the right direction. Still keeping fig. 28 as a reference, an analogue and more evident issue shows up also in image (c) in fig. 29 beneath.

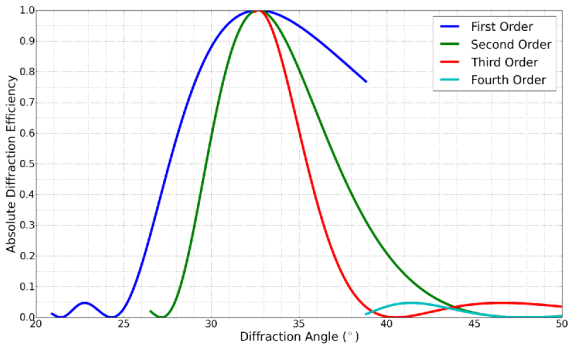

Figure 28 – Analytical graph of eq. (2), applied to our situation.

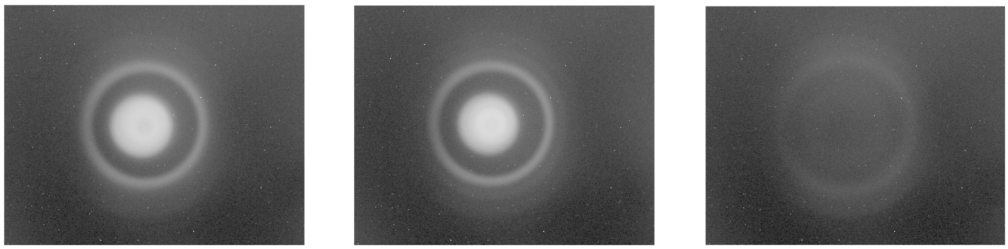

(a) 450 nm, 2nd order; 26/08. (b) 450 nm, 2nd order; 22/08. (c) 300 nm, 3rd order.

Figure 29 – 50 s exposures to three wavelengths. The angle between the arm and the grating normal is about 32.5°.

The first two images of it, (a) and (b), put in evidence the degree of sensitivity owned by the system with respect to the experimental conditions. In fact, they present slightly different ring features, even though they were taken with the same apparatus and method, just four days apart.

4 The Astrophysical Potential of MKIDs

Microwave kinetic inductance detectors are not likely to replace room-temperature semiconductor detectors, like the CCD, in daily use; however, they could make the difference in astronomy. "They will excel in observations of rare, extremely faint sources where every photon matters [like deep extragalactic objects, such as quasars, or exoplanets], and for objects showing fast time variability, like pulsars, magnetic white dwarfs, cataclysmic variables, and low-mass X-ray binaries (LMXBs)" [24]; as regards the optical atmospheric window, in the range 0.3 µm–1 µm. A detailed and extended expected science return for the future KRAKENS is described in [29].

The potential of MKIDs is not limited to the optical: in fact, they can deliver "extremely high sensitivity in the submillimeter" [24]. "The results of the Cosmic Background Explorer (COBE) indicate that 50% of the luminosity and 98% of the photons emitted by the Big Bang fall within the submillimeter and far-infrared (FIR) ranges [...] MUSIC can be used to observe the Sunyaev-Zel'dovich effect in galaxy clusters, dusty star-forming galaxies, and dark matter halos to address fundamental questions regarding the large-scale structure of the universe and the history of star formation over cosmic time" [22]. The FDM will be the crux of their success.

Also in X-ray astronomy, where the atmosphere is almost completely opaque, MKIDs could play an important role. Beyond their multiplexability, their read-out electronics can be operated at room temperature, with the exception of the only cryogenic amplifier: a significant advantage for space applications. "Observations from future X-ray space telescopes will enable tests of Einstein's Theory of General Relativity in the strong-field limit. They will probe the energy generation mechanisms of quasars and stellar-mass black holes. The X-ray emission of distant galaxy clusters will probe the earliest epochs of galaxy formation and large scale structure" [24].

While the way to space is still long, a balloon mission, named PICTURE C and operative in the visible, is scheduled to be launched on two separate flights, in the fall of 2017 and 2019. At the end of this year, the planet finder MEC should see the first light: this is the 20,440-pixel version of the 10,000-pixel DARKNESS—which saw the first light in 2016; they could open the doors to the imaging of exoplanets in the habitable zone, through their reflected light[9]. Incidentally, a duplicate array of DARKNESS will be the target of the instrument that I assembled: with this, the Oxford group is going to demonstrate the feasibility of the first KID-based UV-to-NIR IFS outside the USA, tailored for medium-resolution spectrography of e.g. binary systems. KRAKENS is going to be the future groundbreaking heir of ARCONS, with its 32,400 MKIDs.

4.1 Exoplanets in Sight

In 1584, the Italian philosopher Giordano Bruno (1548–1600) published in London his treatise *De l'infinito universo et Mondi*. From the third of the five included dialogues (twelfth speech):

ELPINO Sono dumque soli innumerabili, sono terre infinite che similmente circuiscono que' soli; come veggiamo questi sette circuire questo sole a noi vicino.

FILOTEO Cossí è.

ELPINO Come dumque circa altri lumi, che sieno gli soli, non veggiamo discorrere altri lumi, che sieno le terre, ma oltre questi non possiamo comprendere moto alcuno; e tutti gli altri mondani corpi (eccetto ancor quei che son detti comete) si veggono sempre in medesima disposizione e distanza?

[9] Self-luminous young planets were the previous targets. Owning a significant gravitational potential energy, a giant one may have a luminosity of 10^{-5} to 10^{-6} $L_\odot$; a few orders of magnitude lower than for a planet in reflected.

FILOTEO La raggione è, perché noi veggiamo gli soli, che son gli più grandi, anzi grandissimi corpi: ma non veggiamo le terre, le quali per esserno corpi molto minori, sono invisibili; come non è contra raggione che sieno di altre terre ancora che versano circa questo sole, e non sono a noi manifeste o per lontananza maggiore o per quantità minore, o per non aver molta superficie d'acqua, o pur per non aver detta superficie rivolta a noi et opposta al sole, per la quale come un cristallino specchio concependo i luminosi raggi si rende visibile.

The era of exoplanets began in 1992, when Dr A. Wolszczan and Dr D. A. Frail announced the discovery of a planetary system around the millisecond pulsar PSR1257 + 12, made with the 305-m Arecibo radio-telescope [17]. Nowadays, almost 3,000 planets have been confirmed outside the Solar System, with a decisive contribution from the space telescope Kepler; some of them are in the fateful habitable zone [7]. Besides looking for bio-signatures out there, what motivates us is to understand the processes that created planets like ours from sub-micron clusters.

A first step in studying extra-solar planets has been taken through transit and (stellar) radial-velocity observations, i.e. thanks to indirect detection methods. Nowadays, we can exploit the confluence of technological advances—e.g. in adaptive optics[10] and imaging detectors—and make the leap to their direct characterisation, through the reflected starlight. Two main knots mark this turning point, which will lead to integrate regions of the exoplanet parameter space inaccessible to the previous techniques. First of all, the overwhelming glare of the host star imposes high contrasts; in parallel, the high spatial resolutions needed are blurred out by turbulences in the Earth's atmosphere, known as seeing. A solution to the former problem is offered by the extreme AO combined with coronagraphy, which is "a really fancy version of sticking your hand over the Sun and looking nearby", as Dr B. A. Mazin had to say. With this pairing, the required fractional planet brightness of a Earth-like planet with respect to a Sun-like star (10^{-10}) is doable, but a limiting "ceiling" is set by "scattered residual starlight that escapes coronagraphic suppression and interferes coherently in the final image plane" [19]: the speckles.

Again, the "high time resolution of MKIDs allows focal-plane speckle nulling at the speed necessary to control atmospheric speckles in real time, and discrimination of speckles from faint companions during post-processing using statistical techniques similar to the "dark speckle" approach. Additionally, the energy resolution of MKIDs allows either form of speckle suppression to be applied as a function of wavelength" [19]. DARKNESS and MEC are going to put all this to the test. The dark speckle technique exploits the fluctuations by destructive interference in the speckle-pattern, over a short exposure, to create a dark map of the focal plane and recognise the steadier flux of the planet, which follows the Poissonian statistics instead of the modified Rician distribution [30]. In fact, these "speckles vary too slowly to average out with long exposures, and too quickly to control in real time with conventional focal-plane detectors or to subtract reliably with differential imaging" [19]. MKIDs are the perfect ingredient, since they lack read noise and dark current, which would affect the statistics. The latter technique is known as spectral differential imaging and could work in combination with the former: it takes advantage of the fact that speckles "move away from the center of the focal plane when observed at longer wavelengths, while astrophysical sources will remain in-place" [19]. Still another technique could be deployed to kill the speckles: it's called coherent differential imaging and uses AO to modulate these and "distinguish them from faint companions whose light is incoherent with the speckles" [19]. Thanks to the intrinsic speed of MKIDs, the full potential of AO would be immediately accessible: instead of a secondary detector, they would enable a focal-plane wave-front control.

[10] A technology that allows to compensate for the atmospheric distortion in the wavefront of radiation. It relies on the instantaneous deformation of the segments composing one of the mosaic mirrors in a telescope dish; these were invented in Bologna by Guido Horn d'Arturo, renowned director of Bologna Observatory from 1921 to 1954.

4.2 New Frontiers with Dragonfly

As a suggestion of mine, one alternative solution to coronagraphy could be a hybrid system between MKIDs and Dragonfly, whose concept is shown in fig. 30. This is a nulling interferometer resulting from a collaboration between Australian Astronomical Observatory, The University of Sydney and Macquarie University: its goal is the extreme-resolution and high-contrast imaging of exoplanets in the NIR H band of the spectrum. The apparatus builds on an integrated astro-photonic chip, which—in analogy with the compound eyes of a dragonfly—is capable of remapping the segmented pupil of a telescope into a pseudo-slit, suitable for a conventional dispersion. Currently, this is fully in charge of some optics; but, MKIDs could replace (part of) it, reducing the complexity of the apparatus. They would be ideal in order to enhance the performances of the Dragonfly project, thanks to their unique time- and energy-resolution capabilities.

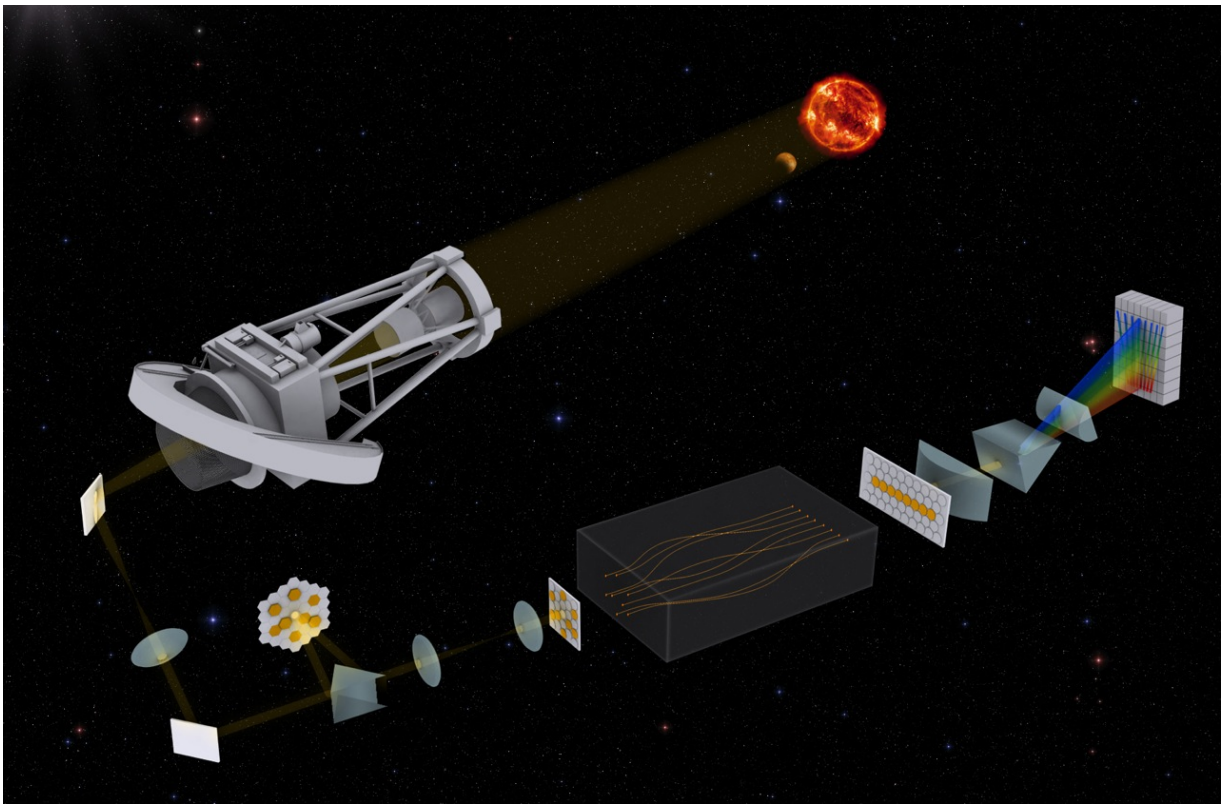

Figure 30 – Artist's impression of the structure of Dragonfly, an integrated pupil-remapping interferometer (IPRI).

In this revised version of aperture masking, there are no speckles: the starlight is suppressed through destructive interference with itself; in practice, through couples of channels set in anti-phase with respect to each other, by means of an achromatic phase shifter. On the other end, the light from the planet enters the telescope off-axis, so it reaches the second channel in delay and is not cancelled out [16]. To be precise, free-space nulling interferometry was performed at the time of fig. 30; whereas, in the modern version of Dragonfly, this occurs via evanescent coupling, in (couples of) the three-dimensional waveguide structures laser-sculpted into the bulk of a dielectric (such a fused silica). This technique converts the redundant aperture of a telescope into an interferometric array. Thus a substantial gain in angular resolution is achieved, allowing to search for the star companion(s) around the $\frac{1.22\lambda}{D}$ diffraction limit—the required star-planet separation for the habitable-zone is around $0.1''$, to give an idea. The price of it is a partial sacrifice of collective area: one more reason to use photon-counting detectors, just like MKIDs.

5 Conclusion

"The CCD has provided new possibilities to visualize the previously unseen. It has given us crystal-clear images of distant places in our universe as well as the depths of the oceans" [5] and of our inner body, in medicine. But, CCDs and its semiconductor variations are reaching the peak of advancement. In parallel, a novel era for optical astronomy is emerging on the horizon, with the advent of powerful telescopes such as the three of the ELT generation. Therefore, innovative technology with greater specific capabilities is desirable, in order to take full advantage of the incoming potential. By efficiently applying the superconducting kinetic inductance effect, instruments of the MKID-family are already intrinsically capable of performing integral-field spectrography with microsecond timing, ideal e.g. for pulsars, as well as low noise and broad passband. Thanks to the current pace of improvement—pixel yield, spectral resolution and quantum efficiency being the most critical—they could attain a major goal in astronomy, within the next decade: the direct characterisation of exoplanets, for which every photon counts.

6 Acknowledgements

Many thanks to my supervisors, within the sub-department of Astrophysics at the University of Oxford. They offered me the opportunity to grow from a scientific point of view, through the ups and downs of hands-on research. Thanks to Dr Kieran Sean O'Brien, the head of our group: his enviable experience and problem-solving capabilities managed to unravel stuck situations several times. Thanks to Dr Sumedh Mahashabde and his impressive practical knowledge, a taste of this is captured in fig. 31: his support was fundamental for the success of my project. Thanks to Dr Barnaby Norris, who introduced me to the Dragonfly project, during my internship at the Australian Astronomical Observatory, and made the suggestion for the final of my thesis.

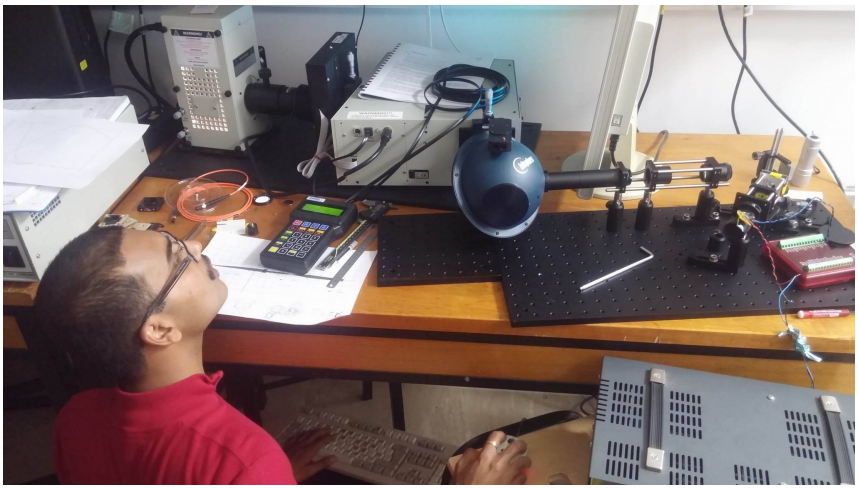

Figure 31 – Dr Mahashabde trying to test the spectrometer with a photodiode. At the end, this sensor was replaced with a CCD camera, which is far more sensitive and easier to handle. On the right, a power supplier is linked to a barely visible circuit—he taught me how to solder it—necessary for the detection, attached to the structure containing the sensor. The circuit is, in turn, connected through a LabJack interface to a computer for the analysis.

Going back from Oxford to Bristol, thanks to Dr Ben Maughan and Dr Rhys Morris, my supervisors for my first serious astrophysics project, where I learnt a lot about CCDs. Without their year-long patience and support, I wouldn't have had the chance to join these two internships. They were my first guides in research and triggered my concrete interest for optical instruments.

Appendices

A Grating Numerical Simulations

To characterise the blazed diffraction grating, I used the software GSolver, in its version 5.2. This builds on a class of algorithms that gives numerical solutions of the vectorial Maxwell's equations involved in the problem. Its working material is a periodic grating structure that lies at the boundary between two homogeneous, linear, isotropic and semi-infinite media [40]. In our case, the choice has fallen on an aluminium substrate and a vacuum superstrate, above that one.

First of all, my supervisor and I adapted a script borrowed from the colleague Dr John Capone, creating a macro that provides enhanced control over the structure and composition of each tooth forming the reflective grating; the code was originally tailored for a transmission one. For our specific situation, I considered 100 layers of the same height, a blaze angle of 8.6° and a groove period of $3.\overline{3}\,\mu m$; this is the inverse of the groove density, which is 300 grooves/mm. When looking at the code attached below, you can refer to fig. 32 and to the following sine law, which contain the same notation: the angles ϕ and γ, there, correspond to *phi* and *gamma*, here. The apex of the saw teeth is manually determined within the macro, setting $apex = 90$ degrees[11].

$$\frac{sin(apex)}{d} = \frac{sin(gamma)}{dh/cos(phi)} \tag{4}$$

The next step was to determine with how many orders is more convenient to feed the simulator, in order to obtain an accurate and efficient computation of the grating absolute diffraction efficiency. This is the reason behind the plot shown in fig. 33. Looking at this, I picked out 10, belonging to the curve's plateau, as the value to select in GSolver; whereupon I performed some numerical simulations of GR25-0310 and produced the plots shown within fig. 34. The mentioned reflective grating that has been deployed lights up—i.e. gives the peak of absolute diffraction efficiency—at the blaze wavelength of 1 µm. According to [39], the absolute efficiency is defined as the radiation intensity relative to the incident one. By contrast, the relative diffraction efficiency refers to the reflection from a polished mirror coated with the same material on the grating top.

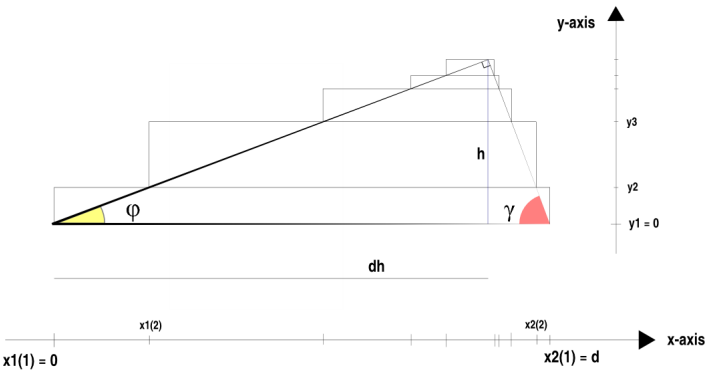

Figure 32 – Profile approximation for a rectangular-apex tooth.

Figure 33 – Behaviour of GSolver when different numbers of orders are considered in the computation of the absolute efficiency. This simulation has been done in the first order, for a wavelength of 1 µm.

[11] For curiosity, an Old Babylonian tablet named Plimpton 322, dated between the 19th and 16th centuries BCE, has been recently interpreted as the world's only exact ratio-based sexagesimal trigonometric table. This replaces Hipparchus' table of chords (II BCE) as the oldest trigonometric table, predating Pythagoras by a millennium [27].

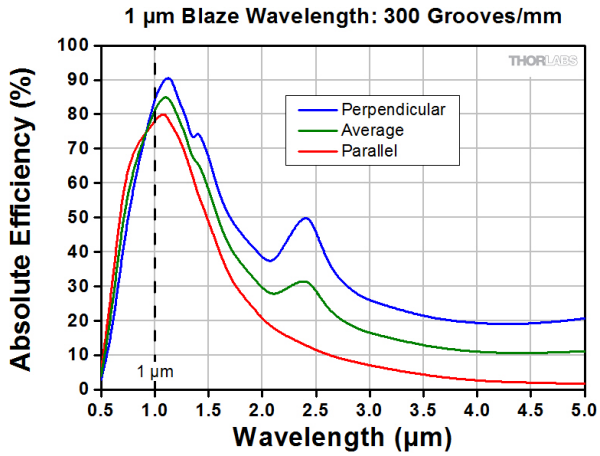

(a) Nominal absolute-efficiency curves [15].

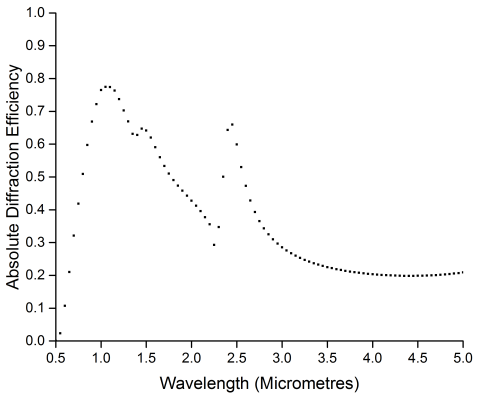

(b) Perpendicular-polarisation scatter plot.

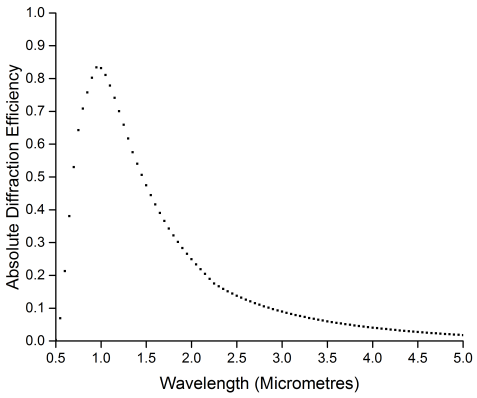

(c) Parallel-polarisation scatter plot.

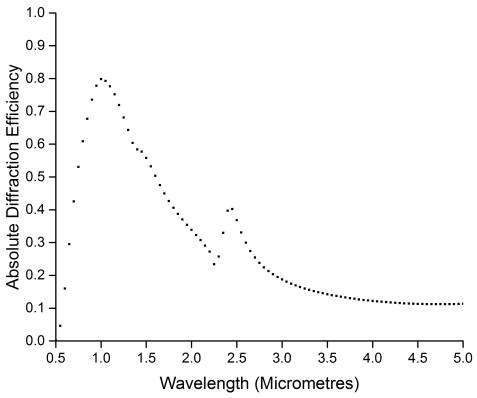

(d) Average-polarisation scatter plot.

Figure 34 – Mosaic where the measurements made by Thorlabs, reported in (a), are compared with my numerical simulations, by considering three characteristic polarisation states of radiation. In (b), (c) and (d), the Littrow configuration is satisfied, and the absolute efficiency maximised, for each wavelength—not only for 1 µm, as in (a).

Made that clear, the profiles of my scatter plots are in reasonable agreement with the nominal graph (a), resulting from the Thorlabs measurements, with the Littrow mounting configuration. While keeping an eye on this reference diagram, you can spot analogue features in the numerical simulations, such as the two secondary bumps in the scatter plot (b): they are anomalies that were first observed by Dr R. W. Wood[12], in 1902, and then explained as the effects of surface plasmon resonance [39]. Plot (d) displays the same small change in slope as well as another bump that stand out also in the central curve of the graph (a). Finally, plot (c) presents the smooth trend expected in case of an electric field oscillates linearly and in parallel with respect to the linear grooves of the ruled grating. For all the three scatter plots, the "1st order Littrow constraint" box had been checked, in GSolver. Therefore, the incidence angle, with respect to the grating normal, had been coupled with the wavelength: in this way, the Littrow configuration for the 1st order is maintained as the wavelength varies within the adopted interval. This is not what happens in reality, but it's useful to highlight the features of each efficiency profile, by enhancing the absolute-efficiency values for every point in the plots and not for the only blaze wavelength.

[12]In 1910, he also produced "the first deliberately blazed diffraction grating" [39], following the intuition of Lord Rayleigh, in 1874, in order to concentrate most of the light in one order, by changing the shape of the grooves.

```
import numpy as np

def get_layers(d, phi, apex, nlayer): # function of groove period (microns), blaze angle (degrees), apex angle (degrees) and number of layers

    phi = np.deg2rad(phi)  # blaze angle, given in degrees and converted to radians
    apex = np.deg2rad(apex)  # apex angle
    gamma = np.pi - phi - apex  # 3rd angle in the tooth

    dh = d * np.sin(gamma) * np.cos(phi) / np.sin(apex)  # base length of the right triangle on the side of theta
    h = dh * np.tan(phi)  # height of tooth

    y = np.linspace(0., h, nlayer + 1)  # layers' vertical profile, with nlayer + 1 generated points
    x1 = y / np.tan(phi)  # distance from the beginning of the layer, for each layer
    x2 = d - y / np.tan(gamma)  # distance from the end of the layer, for each layer

    t1 = x1 / d   # x1 rescaled with respect to the groove period, which become the normalisation factor
    t2 = (x2 - x1) / d  # layer length, rescaled with respect to the groove period
    t3 = 1 - x2 / d   # out-of-the-layer length on the side of gamma, rescaled with respect to the groove period

    hy = y[1:] - y[:-1]  # array with the thickness of each layer (in microns)

    return hy, [t1[:], t2[:], t3[:]]    # useful output of this function

def create_grating(output, block):   # function creating a file, which defines the composition of the blocks constituting the the tooth profile and its surroundings, layer by layer

    hy, t_arr = get_layers(3.3333333, 8.6, 90, 100)  # choose the variables and allocate the output of get_layers

    t_arr = np.array(t_arr)     # just change the format of the array

    if np.shape(t_arr)[0] != len(block):    # if the number of parts (size of the first dimension, [0]) is different from the number of chosen materials, within every layer:
        print("Error: you must specify the material for each block within a layer.")
        return

    # let's round the components of t_arr and assure that, for each layer, the normalised length is 1
    t_arr[0] = np.around(t_arr[0], 3)   # round the array t1 to three decimal places
    t_arr[1] = np.around(t_arr[1], 3)
    t_arr[2] = np.around(t_arr[2], 3)
    t_off = np.around(np.sum(t_arr, axis=0)-1., 3)  # round the array with the component-by-component (along the 0-axis) sum of the three array-
```

```
    components minus 1 as before
39   t_arr -= t_off   # subtract the right operand from the left operand and
    assign the result to left operand (line equivalent to t_arr = t_arr -
    t_off)
40
41   fout = open(output, "w")  #  output file variable opened for writing;
    any file with the same name is erased ("w")
42
43   for i in range(len(hy)):    # loop on the number of layers
44       fout.write("[LAYER]\n")     # \n is to start a new line at the end
    of line written in the file
45       fout.write("{:.3f}\n".format(hy[i]))    # write the thickness of
    each layer in floating point with three digits after the decimal point
46       for j in range(len(block)):    # loop on the number of blocks
47           index_updater = "true"   # flag which tells GSolver to update
    the index value if the wavelength changes
48           if block[j].startswith("CONSTANT"):     # if one of the three
    parts of the layer involved starts with CONSTANT:
49               index_updater = "false"  # flag which tells GSolver NOT to
    update the index value if the wavelength changes
50           fout.write("{:.3f} {} {}\n".format(t_arr[j][i], block[j],
    index_updater))    # write the values in three columns, with different
    formats
51   fout.write("[END]")     # just write end once out of the loop
52
53   fout.close()
54
55 create_grating('Grating_profile.txt', ['CONSTANT Ones', 'Table AL', '
    CONSTANT Ones'])   # it calls the generating function
```

B Main Components of the Spectrometer

All the construction information is collected in the next dimensional diagram, which illustrates a section of the optical apparatus assembled on the optical table. The integrating sphere is loosely connected to the monochromator through a tube, which shields the optical path from external light. Then, in order, there are the three Thorlabs lenses LA1951, LA1131-ML and LA1951, with some hand-made cardboard stops in between. At the end, a fiber illuminates a CCD camera.

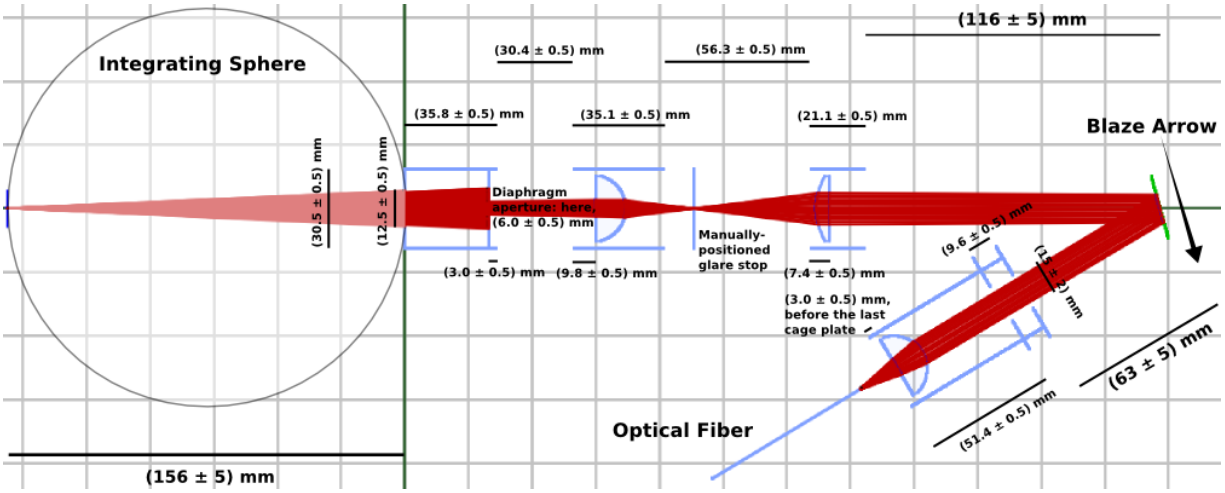

Figure 35 – OpticalRayTracer design of the optical arrangement, with the distance relations between its elements.

Our source of monochromatic electromagnetic radiation is the monochromator 74128, by the Oriel Instruments: this model belongs to the family Cornerstone and has a $f/3.9$ focal ratio, with an effective focal length of 260 mm. It's a fully automated, multi-grating instrument allowing to choose a wavelength that ranges roughly from UV to NIR, with a claimed accuracy of 0.35 nm. In fig. 36, on the left, you can see its dedicated interface, the 74009 Hand Controller; and behind it, attached to the main body of the monochromator, the six-position motorised filter-wheel case.

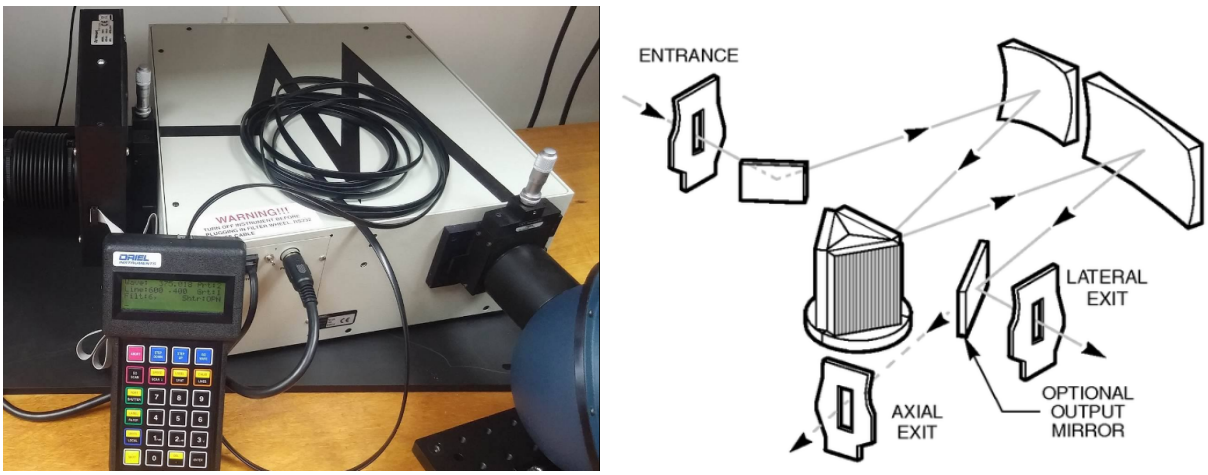

Figure 36 – On the left, the Oriel Cornerstone 260 monochromator 74128 with dedicated hand controller. On the right, its optical configuration, which is based on an asymmetrical in-plane version of the Czerny-Turner design [3].

The monochromator is fed by an incandescent light bulb having a limiting power of 150 W, which we used to push up to 135 W; this is located in an appropriate lamp-housing, before the filter-wheel case. On the other side, the principal arm of the spectrometer starts with an iris diaphragm, attached to the Labsphere integrating sphere. And it ends with our blazed reflective diffraction grating: the model GR25-0310, replicated from a master that had been ruled with a diamond tool, by the company Thorlabs. This is made of a soda-lime glass substrate—giving the characteristic saw-pattern—covered by a thin reflective aluminium coating [15]. The grating has its surface pivoting on the axis of a manual rotating stage, which supports the secondary arm. The stage has a vernier scale with $5'$-markings engraved on its perimeter, which enables us to make measurements of the angular displacement of this arm from the grating normal. The last element of the spectrometer is the multimode optical fiber model M25L02, by Thorlabs, having a numerical aperture of about 0.22. Its core diameter is around 200 µm, reaching 240 µm with the cladding and 400 µm by taking into account also the coating. In fig. 37, you can appreciate the overall assemblage.

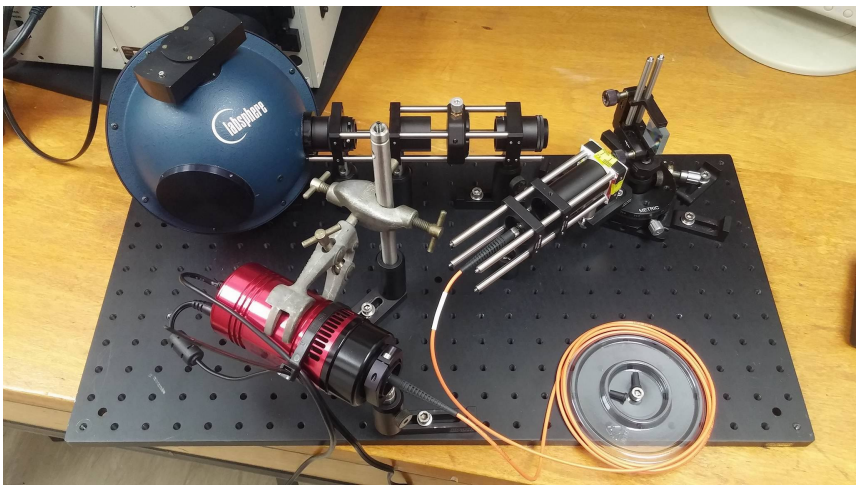

Figure 37 – Overview of the final spectrometer assembled on the optical table. You can refer to the schematic representation of fig. 35 for its internal distances.

C Tolerancing of the Camera Lens

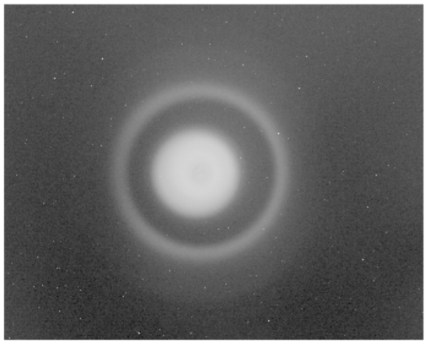

(a) Reference: it's image (a) of fig. 29.

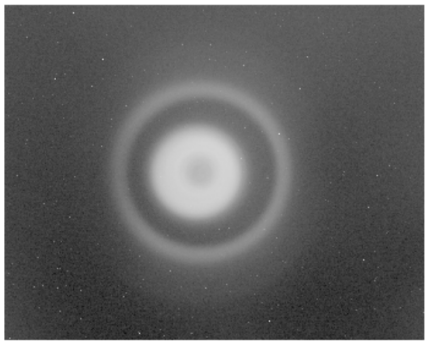

(b) 450 nm, 2nd order; 0.5 mm ahead.

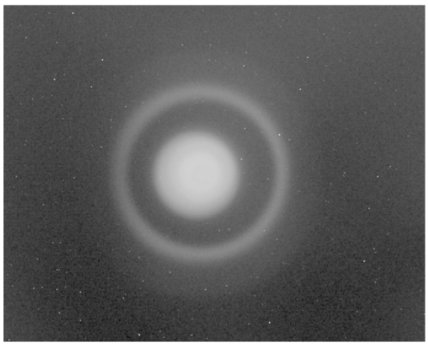

(c) 450 nm, 2nd order; 1 mm backwards.

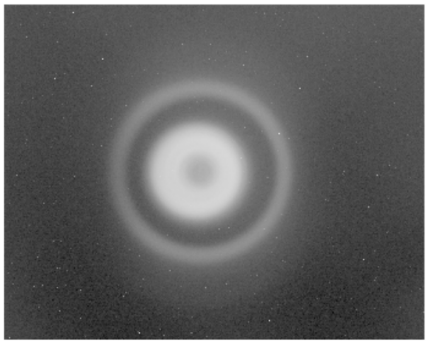

(d) 450 nm, 2nd order; 1 mm ahead.

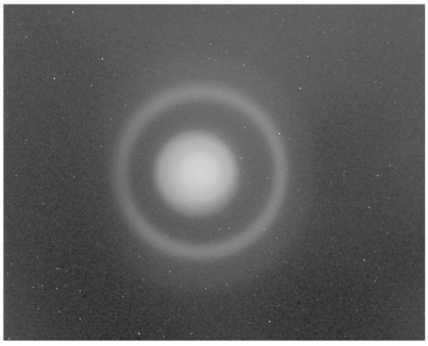

(e) 450 nm, 2nd order; 2 mm backwards.

Figure 38 – Pictures taken with the Atik 460EX camera, through the programme MaxIm DL. The exposure is set to be 50 s for all of them, while the angular distance of the secondary arm from the grating normal is about 32.5°. The light intensity is represented in $\log_{10}$ grey-scale; I've used the application SAOImage DS9 for this conversion.

Let's see what happens when the setup of fig. 29 is slightly varied as of the distance between the fiber input and the focusing lens present in the movable arm. I chose a wavelength of 450 nm. By relocating the cage plate which holds the entrance of the optical fiber nearer to the diffraction grating, the central circle spreads out, leaving an increasingly relevant hole in the centre. Moreover, the main (outer) ring seems to become a bit thicker. These cases could be an effect of the skewer rays being captured by the fiber (cf. fig. 26). (b) and (d) of fig. 38 have to be discarded. On the other hand, moving away from the grating seems to reduce the overall amount of radiation, thus eliminating some skew rays and making the central circle smaller and brighter inside. After this short evaluation, I finally opted for the setup of image (a) as the definitive compromise.

References

[1] Arp H., *Atlas of Peculiar Galaxies*, California Institute of Technology (Caltech), 1966.

[2] *Club of Aficionados in Optical Spectroscopy* (CAOS) website; Optical Fibres section, Characterization of Optical Fibres: http://www.eso.org/~cguirao/caos.

[3] *Cornerstone 260. 1/4-m Monochromator Family*, User's Manual; Oriel Instruments, 2015.

[4] *Crystaltechno* website: http://www.crystaltechno.com/Al_en.htm.

[5] *Award Ceremony Speech by Prof. J. Nordgren*, on December 10, 2009: the Nobel Prize in Physics 2009 was divided, one half awarded to Charles Kuen Kao "for groundbreaking achievements concerning the transmission of light in fibers for optical communication", the other half jointly to Willard Sterling Boyle and George Elwood Smith "for the invention of an imaging semiconductor circuit—the CCD sensor" [11].

[6] *Award Ceremony Speech by Prof. C. W. Oseen*, on December 10, 1929: the Nobel Prize in Physics was awarded to Prince Louis-Victor Pierre Raymond de Broglie "for his discovery of the wave nature of electrons" [11].

[7] *exoplanets.org* website: http://exoplanets.org.

[8] *Horiba* website, Scientific Instruments & Systems: http://www.horiba.com/us/en/scientific/products/optics-tutorial/diffraction-gratings.

[9] *Hubble Space Telescope* website: http://hubblesite.org.

[10] *Mazin Lab* website: http://web.physics.ucsb.edu/~bmazin.

[11] *Nobelprize* website: https://www.nobelprize.org.

[12] *Optics Selection Guide*, by the company Thorlabs: Gratings section, p. 798.

[13] *QSI* website: http://www.qsimaging.com/660-overview.html.

[14] *Shimadzu* website, Optical and Laser Devices; Free Spectral Range paragraph in the Description section: http://www.shimadzu.com/opt/guide/diffraction/06.html.

[15] *Thorlabs* website: https://www.thorlabs.com.

[16] *ESA* website; within the Science & Technology section: http://sci.esa.int/darwin/29719-how-nulling-interferometry-works.

[17] Wolszczan A., Frail D. A., *A planetary system around the millisecond pulsar PSR1257 + 12*, Nature, Vol. **355**, Id. 6356, pp. 145–147, 1992.

[18] Mazin B. A., O'Brien K. S. et al., *ARCONS: A 2024 Pixel Optical through Near-IR Cryogenic Imaging Spectrophotometer*, PASP, Vol. **355**, Id. 933, pp. 1348–1361, 2013.

[19] Meekera S. R., Mazin B. A., Jensen-Clem R. et al., *Design and Development Status of MKID Integral Field Spectrographs for High Contrast Imaging*, Adaptive Optics for Extremely Large Telescopes 4 (AO4ELT4) Conference Proc., Vol. **1**, Id. 1, 2015.

[20] Szypryt P., *Development of Microwave Kinetic Inductance Detectors for Applications in Optical to Near-IR Astronomy*, PhD Thesis in Physics, UCSB, 2017.

[21] Calvo M., *Development of Kinetic Inductance Detectors for the study of the Cosmic Microwave Background Polarization*, PhD Thesis in Physics, University of Rome, 2008.

[22] Duan R., *Instrumentation for Kinetic-Inductance-Detector-Based Submillimeter Radio Astronomy*, PhD Thesis in Physics, Caltech, 2015 (defended in 2013).

[23] O'Brien K. S., Thatte N. and Mazin B. A., *KIDSpec: an MKID based medium resolution integral field spectrograph*, SPIE Conference Proc., Vol. **9147**, Id. 91470G, pp. 1–8, 2014.

[24] Mazin B. A., *Microwave kinetic inductance detectors*, PhD Thesis in Physics, Caltech, 2004. Dr B. A. Mazin was the founder of Mazin Lab, at the core of the MKID revolution.

[25] Mazin B. A., *Microwave Kinetic Inductance Detectors: The First Decade*, AIP Conference Proc., Vol. **1185**, Id. 135, pp. 135–142, 2009.

[26] Casini R., Nelson P. G., *On the Intensity Distribution Function of Blazed Reflective Diffraction Gratings*, JOSA A, Vol. **31**, Id. 10, pp. 2179–2184, 2014.

[27] Mansfield D. F., Wildberger N. J., *Plimpton 322 is Babylonian exact sexagesimal trigonometry*, Historia Mathematica, 2017: https://doi.org/10.1016/j.hm.2017.08.001. It's a corrected proof, so the final citation details still need to be added, before the publication.

[28] De Visser P. J., *Quasiparticle dynamics in aluminium superconducting microwave resonators*, PhD Thesis in Applied Sciences, TU Delft, 2014.

[29] Mazin B. A., Becker G., France K. et al., *Science with KRAKENS*, Keck Science Steering Committee Whitepaper, 19 pp., 2015.

[30] Fitzgerald M. P., Graham J. R., *Speckle Statistics in Adaptively Corrected Images*, ApJ, Vol. **637**, Id. 1, pp. 541–547, 2006.

[31] Jovanovic N., Tuthill P. G., Norris B. et al., *Starlight demonstration of the Dragonfly instrument: an integrated photonic pupil-remapping interferometer for high-contrast imaging*, MNRAS, vol. **427**, Id. 1, pp. 806–815 (2012).

[32] Hand E., *Superconducting detectors offer high-speed astronomy*, Nature, online, 2012.

[33] Harrison G. R., *The echellette grating for the infra-red*, Philos. Mag., Vol. **20** (series 6), Id. 6, pp. 770–778, 1910.

[34] Harrison G. R., *The Production of Diffraction Gratings. I. Development of the Ruling Art*, JOSA, Vol. **39**, Id. 6, pp. 413–426, 1949.

[35] Hockey T., *Biographical Encyclopedia of Astronomers*, Springer, 1st edition of 2007.

[36] Rogalla H., Kes P. H., *100 Years of Superconductivity*, CRC Press, 1st edition of 2011.

[37] Rouse Ball W. W., *A Short Account of the History of Mathematics*, 4th edition of 1908.

[38] Kitchin C. R., *Astrophysical Techniques*, CRC Press, 6th edition of 2014.

[39] Palmer C., Loewen E. G., *Diffraction Grating Handbook*, Newport Corporation, 6th edition of 2005. It's essentially based on the guide, with the same name, written in 1970 by the only Dr E. G. Loewen: this was an emeritus director of the Bausch & Lomb grating laboratory, which first managed, around 1950, to make precision gratings available commercially.

[40] Fluckiger D., *GSolver Version 5.2 User's Guide*, Grating Solver Development Company, 7th edition of 2012. The relative company was founded in 1994 by Dr D. Fluckiger himself.

[41] Birney D. S., Gonzalez G., Oesper D., *Observational Astronomy*, Cambridge University Press, 2nd edition of 2006.

[42] Hecht E., *Optics*, Addison-Wesley, 4th edition of 2002.

[43] Hooke R., *Micrographia: or Some Physiological Descriptions of Minute Bodies Made by Magnifying Glasses. With Observations and Inquiries Thereupon.*, The President, Council and Fellows of the Royal Society of London for Improving Natural Knowledge, 1665.

[44] Kasap S. O., *Optoelectronics and Photonics: Principles and Practices*, Pearson Education, 2nd edition of 2013.

[45] Grimaldi F. M., *Physico-mathesis de lumine, coloribus et iride, aliisque adnexis libri duo*, posthumously published in Bologna, 1665. Its opening proposition reads: "Lumen propagatur seu diffunditur non solùm Directè, Refractè, ac Reflexè, sed etiam alio quodam Quarto modo, Diffractè". In a Modern Latin, the meaning of this last term is «by breaking apart in pieces», with reference to the light waves. According to [35], it was this treatise that attracted Sir Isaac Newton to the study of optics. Later, he and Dr Robert Hooke would use the term "inflexion", introduced by the latter in his [43].

[46] Sweetnam G. K., *The Command of Light. Rowland's School of Physics and the Spectrum*, Memoirs of the American Philosophical Society, Vol. **238**, 2000. The author succumbed suicidally in 1997, so the publication of the book was effected by others.

[47] Feynman R. P., Leighton R. B. and Sands M., *The Feynman Lectures on Physics*, Vol. **1**, Basic Books, online (3rd) edition of 2013, presented by Caltech and "The Feynman Lectures on Physics" website: http://www.feynmanlectures.caltech.edu.

[48] Robinson A., *The Last Man who Knew Everything. Thomas Young, the Anonymous Polymath who Proved Newton Wrong, Explained how We See, Cured the Sick, and Deciphered the Rosetta Stone, Among Other Feats of Genius*, Pearson Education, 1st edition of 2006.

[49] Chromey F. R., *To Measure the Sky. An Introduction to Observational Astronomy*, Cambridge University Press, 1st edition of 2010.